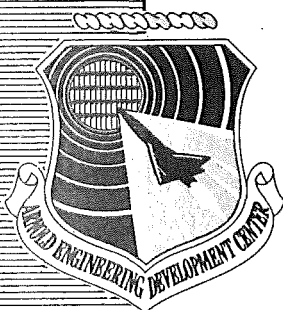


AEDC-TR-76-41



STING DYNAMICS OF WIND TUNNEL MODELS

**VON KÁRMÁN GAS DYNAMICS FACILITY
ARNOLD ENGINEERING DEVELOPMENT CENTER
AIR FORCE SYSTEMS COMMAND
ARNOLD AIR FORCE STATION, TENNESSEE 37389**

May 1976

Final Report for Period July 1, 1974 — June 30, 1975

Approved for public release; distribution unlimited.

Prepared for

**DIRECTORATE OF TECHNOLOGY (DY)
ARNOLD ENGINEERING DEVELOPMENT CENTER
ARNOLD AIR FORCE STATION, TENNESSEE 37389**

NOTICES

When U. S. Government drawings specifications, or other data are used for any purpose other than a definitely related Government procurement operation, the Government thereby incurs no responsibility nor any obligation whatsoever, and the fact that the Government may have formulated, furnished, or in any way supplied the said drawings, specifications, or other data, is not to be regarded by implication or otherwise, or in any manner licensing the holder or any other person or corporation, or conveying any rights or permission to manufacture, use, or sell any patented invention that may in any way be related thereto.

Qualified users may obtain copies of this report from the Defense Documentation Center.

References to named commercial products in this report are not to be considered in any sense as an endorsement of the product by the United States Air Force or the Government.

This report has been reviewed by the Information Office (OI) and is releasable to the National Technical Information Service (NTIS). At NTIS, it will be available to the general public, including foreign nations.

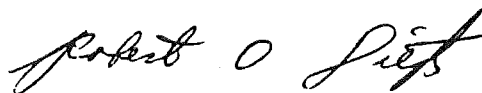
APPROVAL STATEMENT

This technical report has been reviewed and is approved for publication.

FOR THE COMMANDER



KENNETH B. HARWOOD
Major, CF
Research & Development
Division
Directorate of Technology



ROBERT O. DIETZ
Director of Technology

UNCLASSIFIED

20. ABSTRACT (Continued)

transient load inputs. The analysis also provides for sting rigid body motion so that model to tunnel injection and continuous sting rotation (α sweep) can be simulated. A computer program was written to numerically solve the sting-model-balance motion equations. A necessary and supplemental result to the basic analysis was the development of a computer program to compute deflections, first natural frequency, and spring constants for cantilever beams with mixed tapered and untapered section of different materials. Two primary applications of these programs and the associated analysis are given.

UNCLASSIFIED

PREFACE

The work reported herein was conducted by the Arnold Engineering Development Center (AEDC), Air Force Systems Command (AFSC), under Program Element 65807F. The results were obtained by ARO, Inc., (a subsidiary of Sverdrup & Parcel and Associates, Inc.), contract operator of AEDC, AFSC, Arnold Air Force Station, Tennessee. This research was done under Project No. V37A-32A in support of the High Reynolds Number Tunnel (HIRT) Project. The author of this report was James P. Billingsley, ARO, Inc. The manuscript (ARO control No. ARO-VKF-TR-75-150) was submitted for publication on October 13, 1975.

The author gratefully acknowledges the comments, suggestions, and technical information he has received from the VKF HIRT and Tunnel F group personnel. Special thanks are extended to Mr. Jack Coats, Tunnel F Project Engineer, for supplying the detailed technical information required for the Tunnel F application of the present analysis.

CONTENTS

	<u>Page</u>
1.0 INTRODUCTION	7
2.0 ANALYSIS	
2.1 Sting Materials	9
2.2 Sting Deflection, Stress, Strain, and Natural Frequency	11
2.3 Influence Coefficients (Spring Constants)	15
2.4 Sting Natural Frequencies and Mode Shapes	18
2.5 Lagrangian Formulation of Sting-Model Motion Equations	18
3.0 APPLICATIONS	
3.1 HIRT Sting Design and Transient Response	35
3.2 VKF Tunnel F Sting Dynamics	40
4.0 SUMMARY	
4.1 Sting Structural Design	50
4.2 Sting Structural Dynamics	51
REFERENCES	52

ILLUSTRATIONS

Figure

1. Simple Sting Deflection Geometry	7
2. Beam Geometry and Basic Input for STING-1 Program	11
3. Maximum Static Bending Stress in the Sting	13
4. Lowest Natural Frequency of the Example Sting for Various Model Weights and Sting Materials	14
5. Basic Bending Mode Shapes for the Example Carbide-Steel Sting	19
6. Sting Coordinate Systems	
a. Planar Deflection Geometry of the Sting-Model Concentrated Mass Representation	20
b. Coordinates of Mass Element with Respect to Moving Axis Systems	22
c. Coordinates of Mass Element with Respect to an Inertial Axis System	23

<u>Figure</u>	<u>Page</u>
d. Final Coordinates of Deflected Sting with Respect of Undeformed Sting	24
7. Axial Force Bending Moment Schematic	29
8. Predicted Variation of Dynamic Pressure Ratio in a Pilot Ludweig-Tube Wind Tunnel	35
9. Motion History for ATT Model and Steel Sting, Condition No. 7, Basic q_∞ Variation	
a. $\alpha_p = 0.60$ deg.	36
b. $\alpha_p = 0.25, 0.50,$ and 0.75 deg	37
10. Motion History for ATT Model and Carbide-Steel Sting, Condition No. 7, Basic q_∞ Variation, $\alpha_p = 5.0$ deg.	39
11. Motion History for ATT Model and Carbide-Steel Sting, Condition No. 7, $q_\infty = q_{\infty\max}$, $\alpha_p = 5.0$ deg.	39
12. VKF Hypervelocity Tunnel F Stings	
a. Actual Sting Configuration	41
b. Structural Stiffness Synthesis	41
13. Transient Aerodynamic Loads on the Tunnel F Model	42
14. Transient Flow Velocity History for VKF Tunnel F	42
15. Theoretical and Experimental Angular Deflections of the Tunnel F Model	
a. Transient Amplitude without Structural Damping	45
b. Transient Amplitude with Structural Damping	45
c. Average Amplitude	46
d. Oscillation Amplitude	46
16. Theoretical and Experimental Translational Model Nose Tip Deflections	
a. Transient Amplitude without Structural Damping	47
b. Transient Amplitude with Structural Damping	47
c. Average Amplitude	48
d. Oscillation Amplitude	48
17. Model Nose Tip Translational Deflection Geometry	49
18. Theoretical Results for α_{plunge} and Model cg Translation (z_1)	50

TABLES

	<u>Page</u>
1. Characteristics of Sting Construction Materials	10
2. HIRT Sting Deflections and Natural Frequencies . . .	14
NOMENCLATURE.	55

1.0 INTRODUCTION

It is highly desirable to more accurately measure "second-order" aerodynamic effects resulting, for example, from Reynolds number influence. Consequently, all wind tunnel data systems are required to provide a high degree of accuracy. One area that requires thorough analysis is the magnitude of sting bending and oscillations that will exist under high free-stream dynamic pressure and impulse starting loads characteristic of some wind tunnels (Ref. 1).

The majority of aerodynamic data available from wind tunnels is obtained from captive (restrained) model testing. In this situation, the model is supported at the free end of a beam (the sting) which is cantilevered forward from a support sector into the oncoming airflow in the test section. Aerodynamic forces and moments are typically measured with a six-component strain-gage balance located internal to the model. The model is attached to the balance, and the balance is attached to the end of the supporting sting as illustrated in Fig. 1. Both the sting and the balance will deflect under aerodynamic and inertial loads.

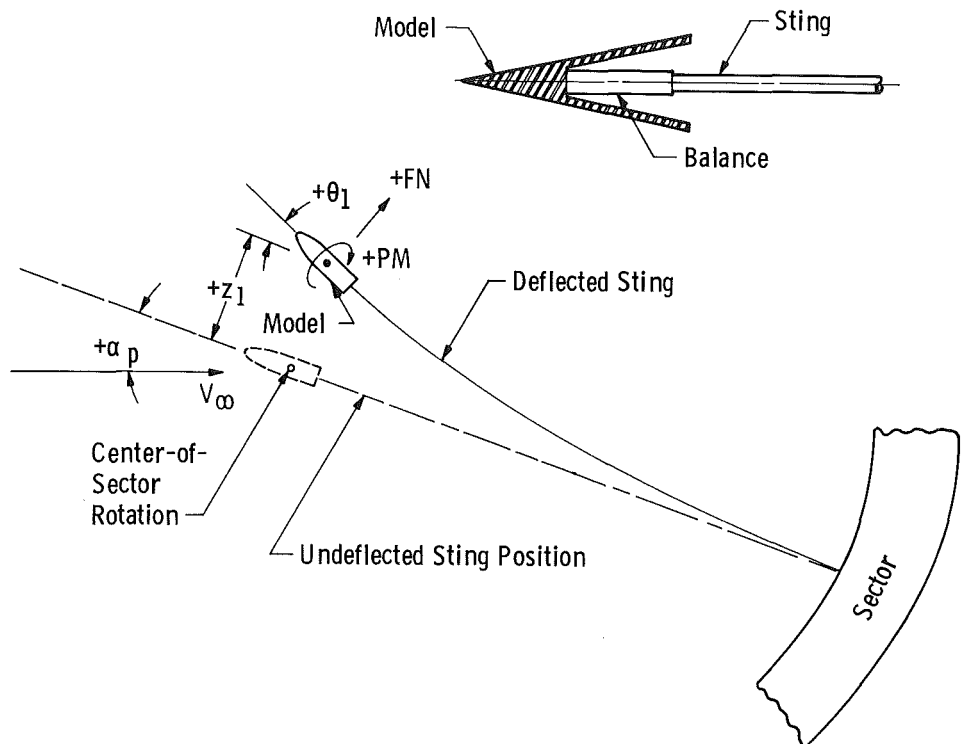


Figure 1. Simple sting deflection geometry.

Many models and stings will be subjected to a rapid application of load during the tunnel starting process and will suffer large static deflections under certain important test conditions due to the magnitude of the load applied. Figure 1 illustrates typical sting deflection geometry. For certain test conditions, the sting tip angular and translational deflection could be several degrees and inches, respectively. These deflections are generally in excess of sting deflections normally encountered in lower dynamic pressure facilities. However, it is not the static deflection alone which causes concern during the portion of the run when data are obtained. The oscillatory deflection of the sting, superimposed on the static deflection which is also present, can have a major influence on the accuracy of steady-state data (Ref. 2).

This investigation was undertaken primarily to evaluate the structural dynamics of sting-model systems subjected to transient load conditions. The results are applicable to existing test conditions such as:

1. Blowdown or Short-Duration Facilities:
The highly impulsive flow conditions create sting oscillations which can influence data acquisition and accuracy and cause structural integrity loss.
2. Facilities Utilizing Model Injection Systems:
The sting-model injection into the tunnel test section under steady flow conditions can create rather large sting deflections. Here, the primary concern is for the sting-balance structural integrity rather than data accuracy.
3. Facilities without Model Injection Systems:
Tunnel starting and stopping loads on the model and sting are particularly severe for transonic and supersonic facilities because of the normal shock which traverses the test section.
4. Testing with Very High Angles of Attack:
High angle-of-attack stall and buffeting of airplane models creates sting transient deflection conditions and the associated previously mentioned problems.

5. Facilities Utilized for Dynamic Stability Testing: During dynamic stability testing for aerodynamic damping derivatives, the basic sting oscillatory motion can be superimposed on the dynamic balance oscillatory motion. This creates data acquisition and accuracy problems (Refs. 3 and 4).

This report discusses various sting materials and describes the analytical techniques utilized to compute sting deflections, spring constants, natural frequencies, and transient motion. Practical utilization of these computational schemes is demonstrated by comparing experimental model sting oscillatory data from a hypersonic impulse tunnel with computed results.

2.0 ANALYSIS

2.1 STING MATERIALS

Slender beam deflection is primarily caused by bending moments, and the deflection is inversely proportional to EI , where E is Young's Modulus and I is the cross-sectional area moment of inertia. Shear deformation is usually less than 1 percent of the total deflection, unless the beam is very short relative to its diameter ($L \approx d$). The allowable bending stress (σ_y) is also a critical beam design item which, for a given moment, is directly proportional to d/I or $1/d^3$.

The wind tunnel test section size limits the model size. The sting-balance cross-section dimensions are dictated by model size limitations and aerodynamic sting-model interference considerations. Since the sting cross-section diameter is thus essentially specified, additional stiffness and lower stress levels cannot always be gained by arbitrarily increasing the diameter and moment of inertia (I). Consequently, any reduction in sting deflection must eventually come from inherent material stiffness parameters, which in this case is obviously Young's Modulus of Elasticity (E).

Traditionally, high strength alloy steels have been the primary structural ingredient for wind tunnel stings and balances. However, in order to combat excessive deflection, other materials, which are stiffer

than steel, warrant serious consideration. Table 1 (Refs. 5, 6, and 7) lists pertinent characteristics of alloy steels and additional materials which are potential candidates for sting construction. It is acknowledged that the alloy steels are cheaper and easier to fabricate, than any of the stiffer materials.

Table 1 indicates that the sintered tungsten-titanium carbide alloys are about three times stiffer than the steels. However, they are somewhat marginal so far as the yield stress (σ_y) is concerned. They also tend to fail in a brittle manner when the yield stress (essentially the elastic limit stress) is exceeded. Even so, they merit serious attention as a primary sting material because of the threefold stiffness increase for cases in which sting deflections pose problems.

Table 1. Characteristics of Sting Construction Materials

<u>Material</u>	<u>$E \times 10^{-6}$ lb/in.²</u>	<u>w, lb/in.³</u>	<u>$\sigma_y \times 10^{-3}$, lb/in.²</u>
Aluminum Alloys*	10.4	0.101	73
Titanium Alloys*	16.0	0.170	170
Nickle-Base Superalloys*	29.0	0.296	175
Steel Alloys*	27.0 to 30.0	0.281	250
Cobalt-Base Superalloys*	33.6	0.320	116
Molybdenum Alloys*	46.0	0.370	125
Tungsten*	59.0	0.700	220
Sintered Tungsten-Titanium Carbide Alloys	90.0** 82.2***	0.525** 0.510***	124****

* Ref. 5

** Ref. 6, Nominal Properties

*** Ref. 6, Conservative Estimate

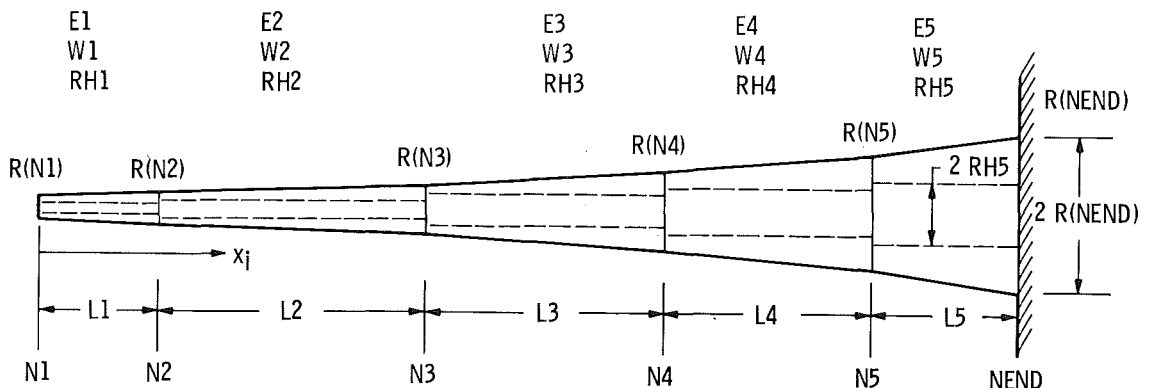
**** Estimated from Weibull's formula (Ref. 7)

2.2 STING DEFLECTION, STRESS, STRAIN, AND NATURAL FREQUENCY

Because of model space limitations and aerodynamic sting-model interference effects, sting configurations normally consist of one or more linearly tapered sections combined with one or more untapered sections. The balance strain-gage lead wires are generally brought out through a hole down the center of the sting. Thus, cross-section dimensions will usually not be uniform throughout the length of the sting. These numerous cross-section discontinuities make closed form integration of the basic slender beam elastic curve equation (Eq. (1)) impractical for realistic stings. The basic slender beam elastic curve equation is

$$\frac{d^2 z}{dx^2} = \frac{M}{EI} \quad (1)$$

where M is the total bending moment at x , and E and I are usually functions of x also. Consequently, numerical integration of Eq. (1) is required for practical sting configurations. Because stings are normally cantilevered from some rigid structure, they are ideally suited for analysis by the first and second area moment propositions (Ref. 8). The area moment analysis was incorporated in a computer program which was written for the cantilever beam schematically illustrated in Fig. 2. This beam has four different cross-section discontinuities. Each section can either be a constant diameter cylinder or a linearly tapered cone



Notes: R(N1)---R(NEND) = Radius at Section Discontinuities
 N1---NEND = Station Numbers at Section Discontinuities
 W1---W5 = Weight/Volume of Material in Each Section
 E1---E5 = Young's Modulus of Material in Each Section
 RH1---RH5 = Radius of Hole through Section

Figure 2. Beam geometry and basic input for STING-1 program.

frustum. Each section may have a hole of arbitrary constant diameter along the centerline. The material of each section is also arbitrary (i. e. steel, aluminum alloys, carbide alloys, etc.). The cross-section shape must be a circle or concentric circles, although this is not a requirement of the basic beam analysis.

This computer program, STING-1, can perform the following calculations after the basic geometric and material properties are provided.

1. Compute deflections (angular and translational) along the beam length caused by the weight of the beam. This information is the static deflection curve of the beam alone and is necessary for the computation of the first natural bending frequency by Rayleigh's Method (Eq. (4)). Maximum bending stress and strain (along the beam length) caused by beam weight are also computed by the following standard relations, respectively:

$$\sigma_b = \frac{Mc}{I} \quad (2)$$

$$\epsilon_b = \frac{\sigma_b}{E} \quad (3)$$

2. Deflection, stresses, and strain caused by concentrated loads or moments at any station along the beam may be computed. In addition to obvious design applications, the deflections caused by concentrated loads are necessary to compute the beam spring constants or influence coefficients (see Section 2.3). Figure 3 shows bending stresses for a sting with a concentrated load of 24,000 lb at one end computed by Code STING-1. Table 2 lists deflections for steel, carbide, and a composite carbide-steel (C-S) sting computed by STING-1 for these same conditions.

3. The first natural frequency may be computed by Rayleigh's Method (Ref. 9). The effect of concentrated masses (the model for instance) can also be included. The expression for the sting natural frequency is

$$\omega_1^2 = \frac{\int_0^L \frac{M^2 dx}{EI}}{\int_0^L z^2 dm + \sum_{i=1}^n \frac{W_i}{g} z_i^2} \quad (4)$$

where M is the total bending moment (including beam weight and concentrated weights) at station x , z is the static deflection at station x , z_i is the static deflection at the concentrated weight locations (x_i), and dm

is the differential mass of the beam at station x . When the static deflection curve is used in Eq. (4), the computed frequency will be slightly higher than if the true dynamic deflection curve is used. This occurs because the small deviation of the static deflection from the first mode dynamic deflection imposes some constraint which makes the beam more rigid and its frequency higher. This is illustrated in Fig. 4 where frequencies for the carbide-steel (C-S) sting are given; both for the Rayleigh method with static deflection and the analysis of Section 2.4 where the true dynamic mode deflection shape is computed. A comparison shows that the Rayleigh method frequency is approximately 6 percent greater than the true dynamic mode frequency. Figure 4 also illustrates the influence of material and model weight on sting natural frequency. The natural frequency of mono-material beams (without concentrated weights) scales according to:

$$\frac{\omega_1}{\omega_2} = \sqrt{\frac{E_2 w_1}{E_1 w_2}} \tag{5}$$

Using material properties from Table 1,

$$\frac{\omega_{\text{Carbide}}}{\omega_{\text{Steel}}} = \sqrt{\frac{(90)(10^6)(0.281)}{(30)(10^6)(510)}} = 1.28$$

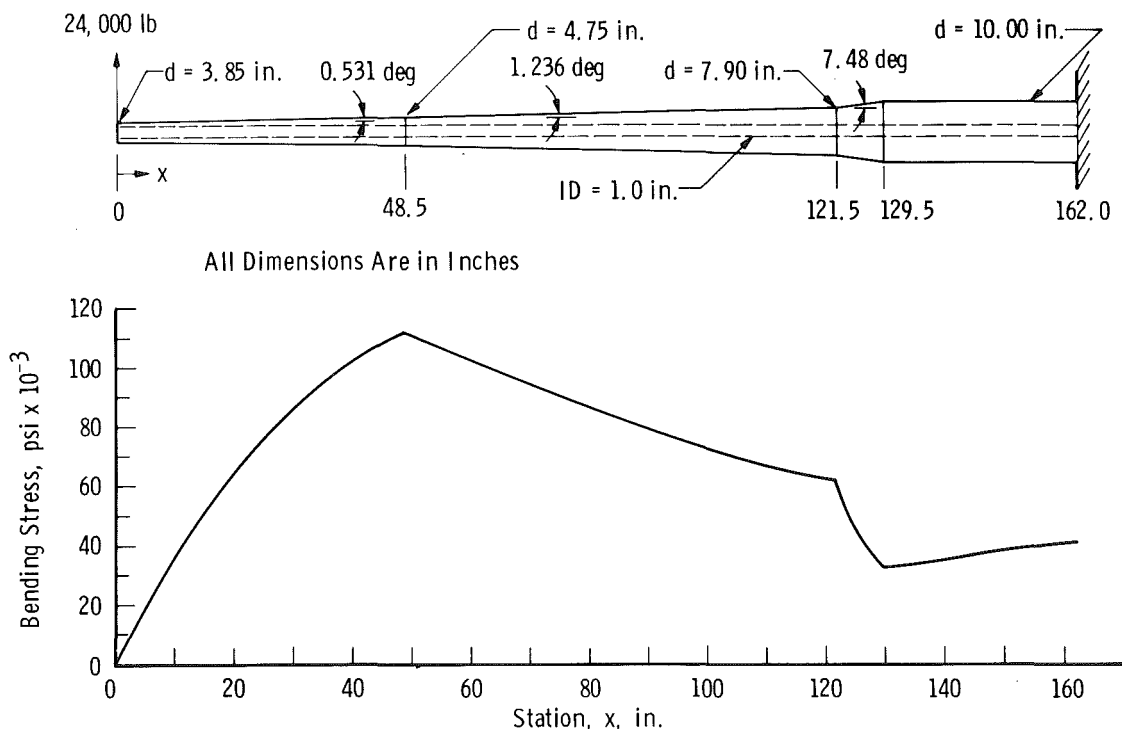


Figure 3. Maximum static bending stress in the sting.

Table 2. HIRT Sting Deflections and Natural Frequencies

Material	End Rotation, deg	End Deflection, in.	Frequency, cps (Fig. 4, $W_M = 0$)
Steel	7.37	8.30	17.0
Carbide	2.47	2.74	21.5
Composite (Steel and Carbide)	2.88	3.81	16.0

To compute the above information, the following material properties were used:

Material	E , lb/in. ²	w , lb/in. ³
Steel	$30(10^6)$	0.281
Carbide	$90(10^6)$	0.525

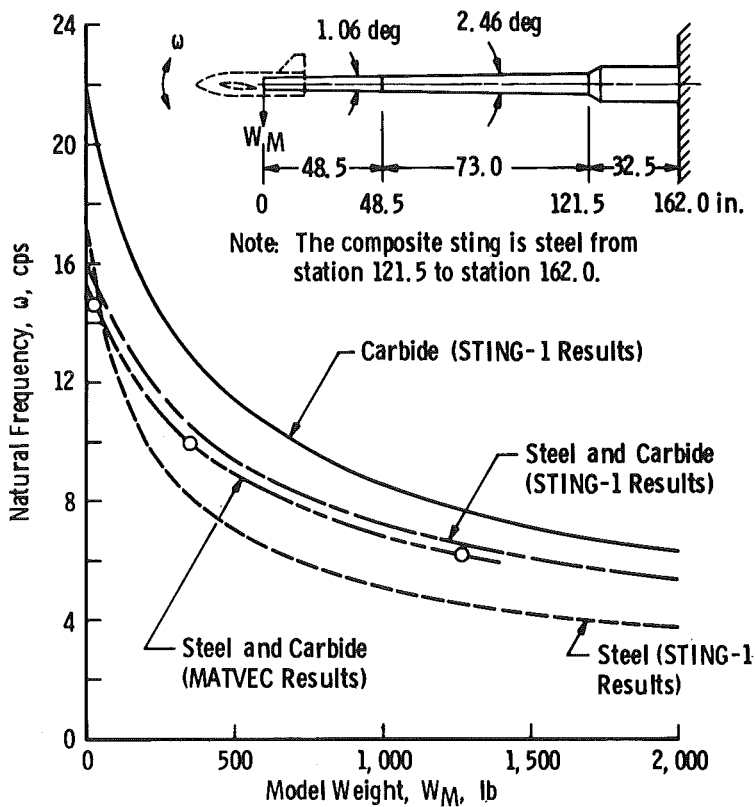


Figure 4. Lowest natural frequency of the example sting for various model weights and sting materials.

The ratio from the more exact Eq. (4) ($W_M = 0$) is:

$$\frac{\omega_{\text{Carbide}}}{\omega_{\text{Steel}}} = \frac{21.5}{17.0} = 1.26$$

4. Certain structural dynamic analyses require the beam to be considered as a series of lumped masses connected by springs. The selection of a particular beam portion or section to form a concentrated mass is a decision requiring some discretion for best results. Once the partitioning selection is made, the STING-1 program will compute the value of the lumped mass (m_i), its mass moment of inertia (I_{y_i}), and its centroidal position (x_i). This centroidal position is the point at which concentrated unit loads and moments will normally be applied to compute the beam spring constants or influence coefficients.

2.3 INFLUENCE COEFFICIENTS (SPRING CONSTANTS)

The structural dynamic analysis described in the next two sections represents the sting-balance-model system as a series of "lumped masses" or concentrated masses. These masses are considered to be connected together by flat weightless springs. A load applied to one mass will influence the deflection of the other masses because of the spring connections. Consequently, the associated spring constants have become known as structural influence coefficients.

References 10 (pp. 17-22), 11 (pp. 19-27), and 12 contain excellent discussions on structural influence coefficients which basically can be classified in one of two categories as:

1. Flexibility influence coefficients, defined by:

$$q_i = \sum_{j=1}^N C_{ij} Q_j \quad (6a)$$

where

- N = number of generalized forces applied
- q_i = deflection (translational or rotational) at point i
- Q_j = Forces (or moments) applied at point j
- C_{ij} = flexibility influence coefficients
= deflection/unit load

Equation (6a) can be written in matrix form as follows:

$$\begin{bmatrix} q_1 \\ q_2 \\ - \\ - \\ q_N \end{bmatrix} = \begin{bmatrix} C_{11} & C_{12} & \cdots & C_{1N} \\ C_{21} & C_{22} & \cdots & C_{2N} \\ - & - & \cdots & - \\ - & - & \cdots & - \\ C_{N1} & C_{N2} & & C_{NN} \end{bmatrix} \begin{bmatrix} Q_1 \\ Q_2 \\ - \\ - \\ Q_N \end{bmatrix} \quad (6b)$$

Basically, C_{ij} , corresponding to the location of the lumped masses of the beam, can be computed from the deflection (translational and rotational) caused by unit concentrated loads or moments applied at the various lumped mass cg locations (x_i).

For computational purposes, it is important to note the four different types of elements which make up the C_{ij} matrix (see Ref. 10, p. 22). The C_{ij} matrix can be partitioned as follows:

$$\begin{bmatrix} C_{ij} \end{bmatrix}_N = \begin{bmatrix} \begin{bmatrix} CTF_{ij} \end{bmatrix}_n & \begin{bmatrix} CTM_{ij} \end{bmatrix}_n \\ \begin{bmatrix} CAF_{ij} \end{bmatrix}_n & \begin{bmatrix} CAM_{ij} \end{bmatrix}_n \end{bmatrix}_{N=2n} \quad (7)$$

where

CTF_{ij} = translational deflection at i caused by unit force at j , ft/lb

CTM_{ij} = translational deflection at i caused by unit moment at j , ft/(ft-lb) = 1/lb

CAF_{ij} = angular deflection at i caused by unit force at j , rad/lb or 1/lb

CAM_{ij} = angular deflection at i caused by unit moment at j , rad/(ft-lb) or 1/(ft-lb)

This allows C_{ij} to be computed by systematic application of the STING-1 program to each of the concentrated mass positions.

2. Stiffness Influence Coefficients, given by

$$Q_i = \sum_{j=L}^N K_{ij} q_j \quad (8a)$$

where

- q_j = deflection (translational or rotational) at point j
 Q_i = force (or moment) applied at point i
 K_{ij} = stiffness influence coefficients
 = load/deflection

In matrix form, Eq. (8a) is written as

$$\begin{bmatrix} Q_1 \\ Q_2 \\ - \\ - \\ Q_N \end{bmatrix} = \begin{bmatrix} K_{11} & K_{12} & \cdots & K_{1N} \\ K_{21} & K_{22} & & K_{2N} \\ \text{-----} & & & \\ \text{-----} & & & \\ K_{N1} & K_{N2} & & K_{NN} \end{bmatrix} \begin{bmatrix} q_1 \\ q_2 \\ - \\ - \\ q_N \end{bmatrix} \quad (8b)$$

Note that K_{ij} is completely analogous to the spring constant, $K = \text{lb/in.}$ employed in one-dimensional spring analysis.

The K_{ij} coefficients are difficult to compute directly from beam theory. Consequently, they are generally computed by inverting the C_{ij} matrix. This is the manner K_{ij} was obtained in the present analysis:

$$[K_{ij}] = [C_{ij}]^{-1} \quad (9)$$

Another important property of the C_{ij} and K_{ij} matrices is that both are symmetric. The C_{ij} matrix as computed by STING-1 was not symmetrical after the third or fourth decimal places (round off error, approximation, etc.). Thus C_{ij} had to be made symmetric so that it would properly invert and yield the following multiplication check:

$$[C_{ij}][K_{ij}] = [I] \quad (10)$$

where $[I]$ is the identity matrix

It is important to note that the C_{ij} coefficients can be determined experimentally (Ref. 12). In fact, this is preferable to computing them analytically and may be absolutely necessary for complex structures.

In any case, some experimental C_{ij} data are valuable for verifying and complementing theoretical results. The VKF balance calibration laboratories currently measure deflection under loads applied at the model attachment point so that static sting rotation from model airloads may be accounted for in data reduction. This type of experimental information was essential to the application which will be discussed in Section 3.2.

2.4 STING NATURAL FREQUENCIES AND MODE SHAPES

The first natural bending frequency may generally be computed with sufficient engineering accuracy by the Rayleigh method as indicated in Section 2.2. For design purposes, primarily to avoid resonance conditions, the higher natural frequencies are occasionally required. Reference 9 (pp. 169-170) outlines a procedure by which the influence coefficient (CTF_{ij}) in conjunction with the lumped mass concept can be utilized to compute the first and higher natural steady-state bending frequencies and mode shapes. From Section 2.3, the CTF_{ij} coefficients are defined as translational normal deflections at x_j caused by a unit force applied at x_i . The final matrix formulation is:

$$\begin{bmatrix} CTF_{11}m_1 & CTF_{12}m_2 & \cdots & CTF_{1n}m_n \\ CTF_{21}m_1 & CTF_{22}m_2 & \cdots & CTF_{2n}m_n \\ \cdots & \cdots & \cdots & \cdots \\ CTF_{n1}m_1 & CTF_{n2}m_2 & \cdots & CTF_{nn}m_n \end{bmatrix} \begin{bmatrix} z_1 \\ z_2 \\ - \\ z_n \end{bmatrix} = \Lambda \begin{bmatrix} z_1 \\ z_2 \\ - \\ z_n \end{bmatrix} \quad (11)$$

where $\Lambda = 1/\omega^2$. This is the standard matrix eigenvalue problem where Λ is the eigenvalue and the associated eigenvectors (z_i) define that particular normalized mode shape. Once the $[CTF_{ij}m_i]$ matrix is formulated, the eigenvalues (frequencies) and associated eigenvectors (normalized mode shapes) may be computed by the MATVEC program (Ref. 13). Concentrated weights such as the model may also be taken into account by proper modification of the appropriate m_i (see Figs. 4 and 5 for MATVEC results for the C-S sting). The mode shapes illustrated in Fig. 5 are typical for cantilever beams.

2.5 LAGRANGIAN FORMULATION OF STING-MODEL MOTION EQUATIONS

Sting-balance-model systems tested in blowdown or short-duration wind tunnels are exposed to transient aerodynamic loads which can act

on both model and sting. Since useful data taking time is limited, modern blowdown facilities are designed to vary the sting pitch angle (α_p) during the run so that the quantity of data obtained is increased. Continuous-flow tunnels may also have this capability for similar reasons. In addition to sector transient rotation capabilities, some modern facilities are capable of translating the sting-model from a location outside the test section into the flow field of the test section via a so-called "injection" system.

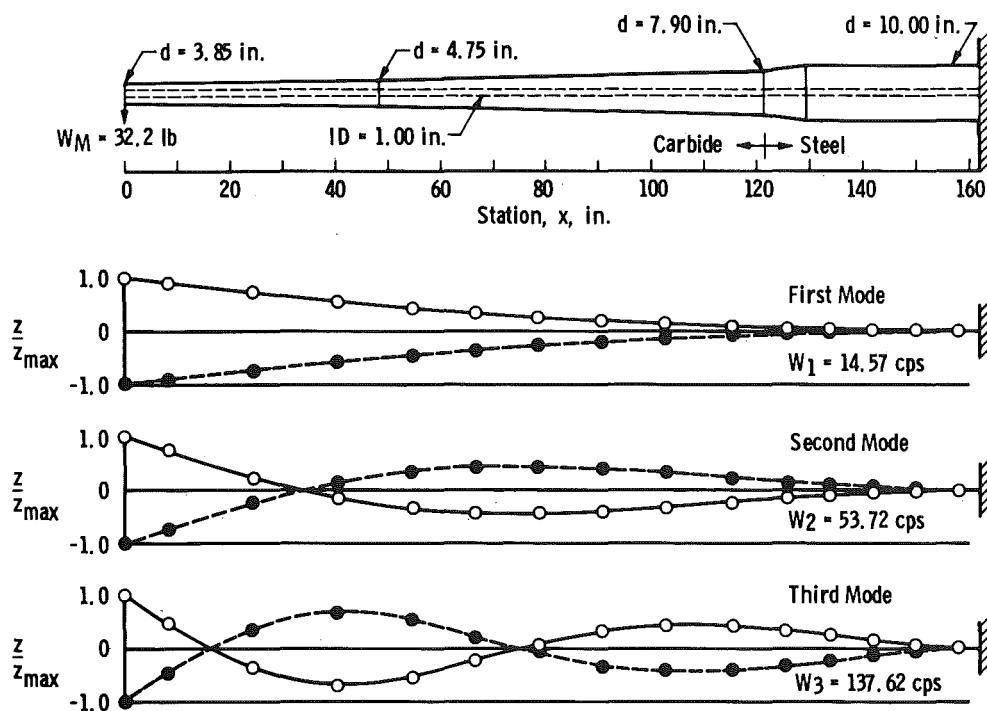


Figure 5. Basic bending mode shapes for the example carbide-steel sting.

Consequently, any realistic analysis of sting structural dynamics must account for elastic deflection of the system caused by:

1. Transient air loads on both model and sting.
2. Transient loads associated with rigid body motion of the system.

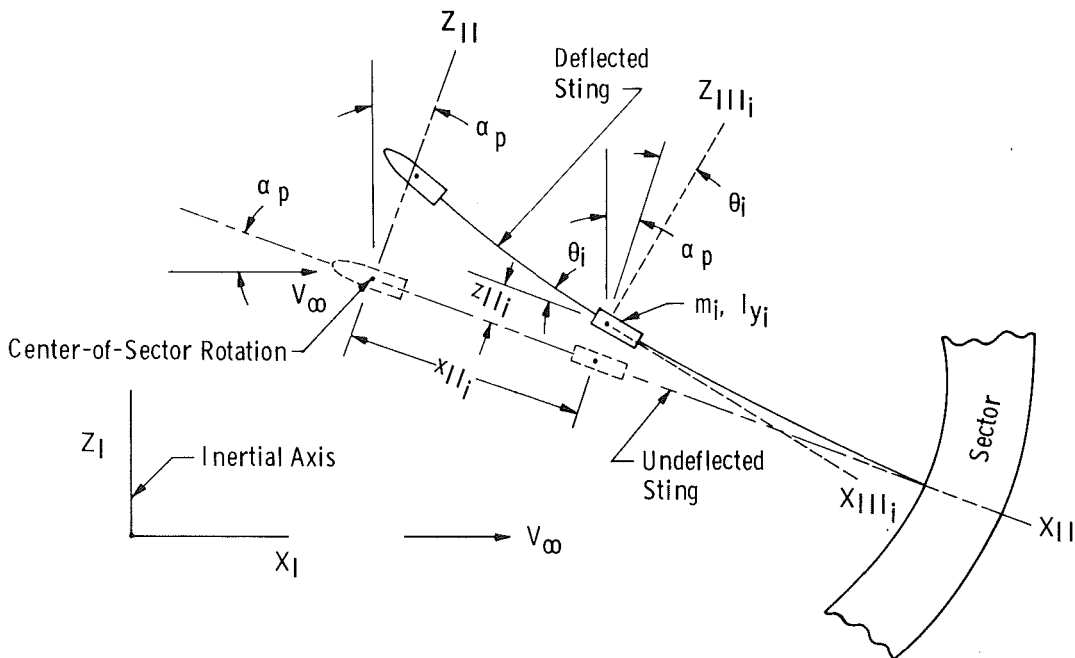
To investigate the general transient planar motion of a sting-model system, it has been represented by a series of concentrated masses as illustrated in Fig. 6a. These concentrated masses are connected by springs so that the motion of one mass influences the motion of the

other masses. Because of the rigid body motion of the sting, it is necessary to employ three basic axis systems which are illustrated in Fig. 6:

- X_I, Z_I Inertial axis, X_I is parallel to V_∞ .
- X_{II}, Z_{II} This axis is fixed to the undeflected sting and moves with it as shown.
- X_{III_i}, Z_{III_i} This axis is fixed to the i th concentrated mass and moves with it as shown.

Lagrange's formulation of dynamics (Refs. 14 and 15) is employed to derive the equations of motion for the i^{th} mass. Lagrange's method provides a methodical and systematic approach which is especially valuable in the present application involving two moving non-inertial coordinate systems.

The present formulation is an extension to the example of the cantilever beam and single concentrated mass given in Ref. 11 (pp. 40-41). The present analysis is also similar, in some respects, to the classical example of airfoil flutter given in Ref. 11 (pp. 210-212) and Ref. 10 (pp. 532-536) where Lagrange's formulation is employed.



a. Planar deflection geometry of the sting-model concentrated mass representation
 Figure 6. Sting coordinate systems.

2.5.1 General Lagrange Equation

The Lagrangian formulation of dynamics provides a systematic approach that gives directly the equations of motion in whatever coordinate system may be convenient (Ref. 14). Application of Lagrange's procedure is remarkably straightforward even for relatively complex systems involving moving non-inertial coordinate systems. Lagrange's basic equation is

$$\underbrace{\frac{d}{dt} \left(\frac{\partial T}{\partial \dot{q}_k} \right) - \frac{\partial T}{\partial q_k}}_{\text{Inertial forces (or moments)}} + \underbrace{\frac{\partial U}{\partial q_k}}_{\text{Conservative forces (or moments)}} = \underbrace{Q_k}_{\text{Non-conservative forces (or moments)}} \quad (12)$$

where:

$k = 1 \dots N$

$N = 2n$

N = number of degrees of freedom or independent coordinates

n = number of lumped masses in the system representation

q_k = generalized independent coordinate. In the present analysis, q_k will either be angular rotation or a linear translation distance, both of which are easily visualized physical quantities. The motion direction specified by Eq. (12) is in the exact direction associated with q_k (Ref. 15, pp. 157-158)

T = total kinetic energy of system and must be measured relative to an inertial axis system (Ref. 14, p.33)

U = potential energy of the system. In the present application, U is the work done by the sting acting as an elastic spring.

Q_k = non-conservative generalized applied force (or moment) acting on the i^{th} mass, (m_i) corresponding to the k^{th} generalized coordinate. In this application, Q_k is primarily of aerodynamic origin.

t = time, sec

The appropriate formulations of T , U , and Q_k are given in the following sections.

2.5.2 The Kinetic Energy and Its Derivatives

In applying Eq. (12) to the sting-model system of concentrated masses as represented in Fig. 6, a very crucial item is the evaluation of the total kinetic energy and its associated derivatives. These yield the inertial forces (or moments) of the system. The total kinetic energy for this system is

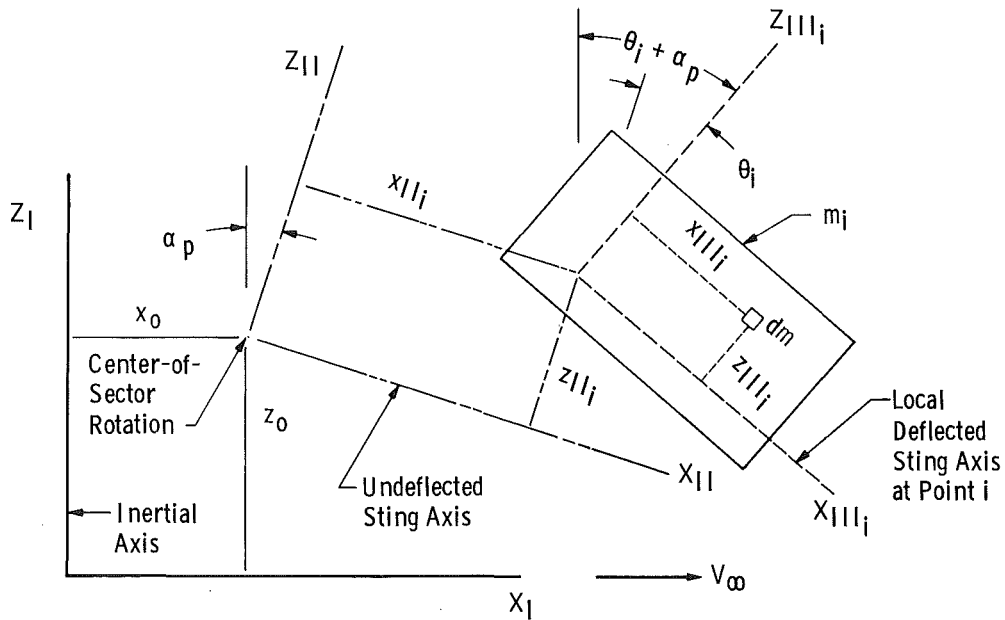
$$T = \sum_{i=1}^n T_i \quad (n = \text{number of masses}) \quad (13a)$$

$$T_i = \frac{1}{2} \int_{m_i} V_{abs}^2 dm \quad (13b)$$

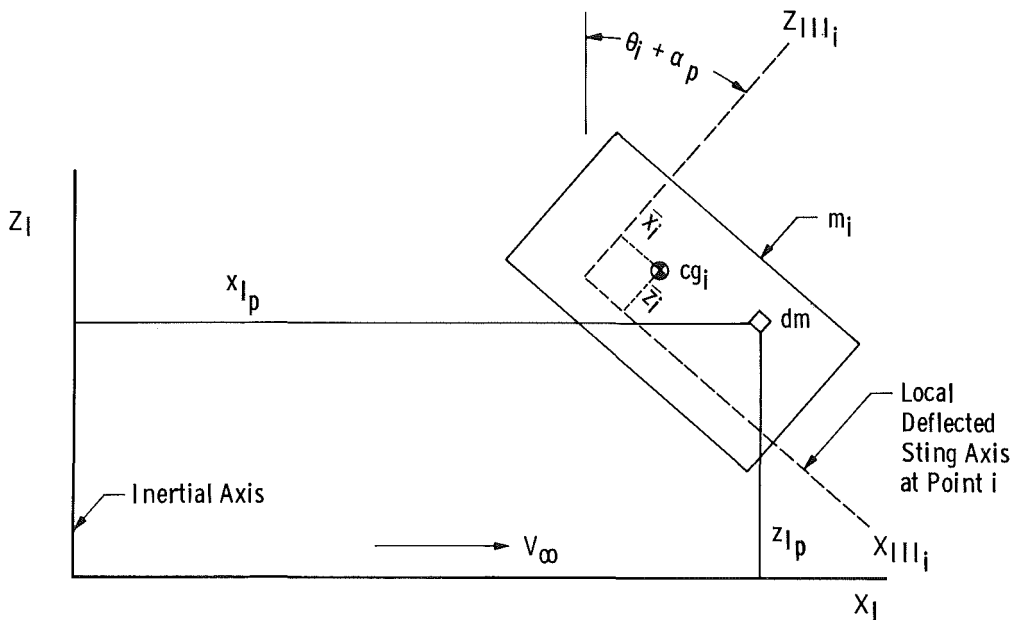
T_i is the kinetic energy of the mass (m_i) and V_{abs} is the absolute velocity of an element of mass (dm), which is located as shown in Figs. 6b and c with respect to the inertial axis (X_I, Z_I). The coordinates of the particle (dm) with respect to the X_I, Z_I origin are

$$x_{I_p} = x_o + x_{II_i} \cos \alpha_p + z_{II_i} \sin \alpha_p + x_{III_i} \cos (\alpha_p + \theta_i) + z_{III_i} \sin (\alpha_p + \theta_i) \quad (14a)$$

$$z_{I_p} = z_o - x_{II_i} \sin \alpha_p + z_{II_i} \cos \alpha_p - x_{III_i} \sin (\alpha_p + \theta_i) + z_{III_i} \cos (\alpha_p + \theta_i) \quad (14b)$$



b. Coordinates of mass element with respect to moving axis systems
Figure 6. Continued.



c. Coordinates of mass element with respect to an inertial axis system
Figure 6. Continued.

Differentiating Eq. (14) with respect to time yields the absolute velocity components of the particle (dm). Note that \dot{x}_{III_i} and $\dot{z}_{III_i} = 0$ since the X_{III_i}, Z_{III_i} axis is fixed relative to mass (m_i) and rotates with it through the angle $(\alpha_p + \theta_i)$. The origin of the X_{III_i}, Z_{III_i} axis is not necessarily the center of gravity of the mass (m_i) (Fig. 6c). Note also that x_{II_i} is a constant distance which denotes the location of the X_{III_i}, Z_{III_i} axis origin along the sting length. Strictly speaking, x_{II_i} does vary slightly as the sting deflects under load, but this very small change will be neglected. The final relation for the total kinetic energy is

$$\begin{aligned}
 T = \sum_{i=1}^n \{ & \frac{1}{2} [\dot{x}_o^2 + \dot{z}_o^2 - 2\dot{x}_o \dot{x}_i \dot{a}_p \sin \alpha_p - 2\dot{z}_o \dot{x}_i \dot{a}_p \cos \alpha_p + x_i^2 \dot{a}_p^2 \\
 & + 2\dot{q}_i (\dot{x}_o \sin \alpha_p + \dot{z}_o \cos \alpha_p - x_i \dot{a}_p) + \dot{q}_i^2 + 2q_i (\dot{x}_o \dot{a}_p \cos \alpha_p \\
 & - \dot{z}_o \dot{a}_p \sin \alpha_p) + q_i^2 \dot{a}_p^2] m_i - [\dot{x}_o \sin (\alpha_p + q_{i+n}) + \dot{z}_o \cos (\alpha_p + q_{i+n}) \\
 & + (\dot{q}_i - x_i \dot{a}_p) \cos (q_{i+n}) + q_i \dot{a}_p \sin (q_{i+n})] (\dot{a}_p + \dot{q}_{i+n}) (\bar{x}_i m_i) \\
 & + [\dot{x}_o \cos (\alpha_p + q_{i+n}) - \dot{z}_o \sin (\alpha_p + q_{i+n}) - (\dot{q}_i - x_i \dot{a}_p) \sin (q_{i+n}) \\
 & + q_i \dot{a}_p \cos (q_{i+n})] (\dot{a}_p + \dot{q}_{i+n}) (\bar{z}_i m_i) + \frac{1}{2} (\dot{a}_p + \dot{q}_{i+n})^2 I_{y_i} \} \quad (15)
 \end{aligned}$$

where

$$q_i = Z_{II_i} = z_i \quad (\text{see Fig. 6d}) \quad (16a)$$

$$q_{i+n} = \theta_i \quad (\text{see Fig. 6d}) \quad (16b)$$

$$x_i = x_{II_i} \quad (\text{see Fig. 6d}) \quad (16c)$$

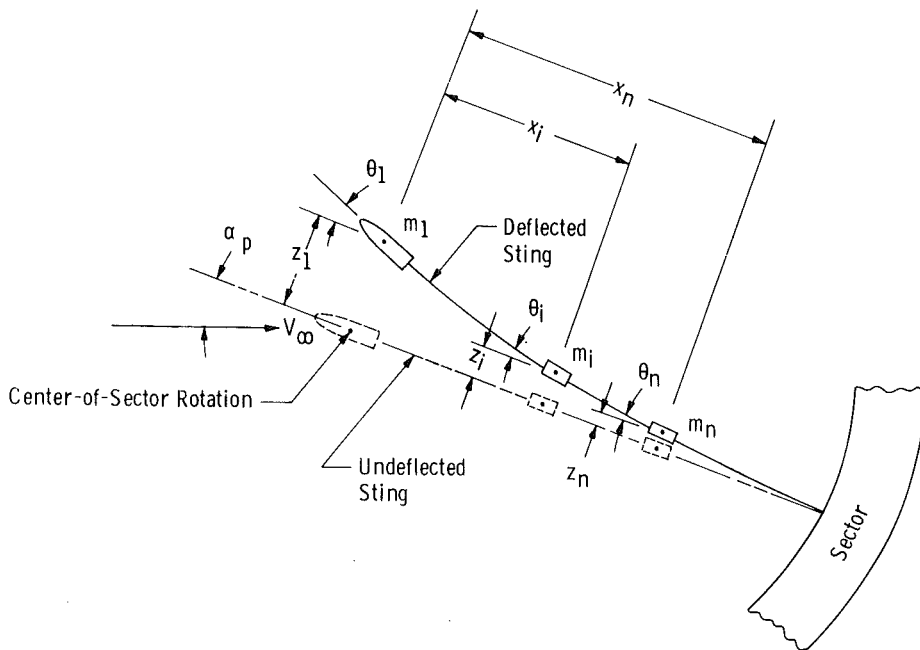
$$\int_{m_i} dm = m_i \quad (17a)$$

$$\int_{m_i} x_{III_i} dm = \bar{x}_i m_i \quad (\text{see Fig. 6c}) \quad (17b)$$

$$\int_{m_i} z_{III_i} dm = \bar{z}_i m_i \quad (\text{see Fig. 6c}) \quad (17c)$$

$$\int_{m_i} (x_{III_i}^2 + z_{III_i}^2) dm = I_{y_i} \quad (17d)$$

Note that \dot{x}_O and \dot{z}_O are the translational velocities of the model support system moving as a rigid body. This motion will occur, for instance, when a model is injected into a wind tunnel on a system in which the model, sting, and support translate in unison.



d. Final coordinates of deflected sting with respect to undeflected sting
Figure 6. Concluded.

It is shown in Ref. 11 that

$$\begin{aligned}
 \frac{\partial U}{\partial q_i} &= \sum_{j=1}^n K_{ij} q_j \\
 &= K_{i1} q_1 + K_{i2} q_2 + \dots + K_{iN} q_N \\
 &= Q_i \\
 &= \text{Force (or moment) at point } i \text{ in the} \\
 &\quad \text{direction of } q_i \text{ (see Eq. (7a))}
 \end{aligned}
 \tag{20}$$

In the present formulation,

$$\begin{aligned}
 \frac{\partial U}{\partial q_i} &= \sum_{j=1}^{2n} K_{ij} q_j \\
 &= \text{Sting elastic restoring force at point } x_i
 \end{aligned}
 \tag{21a}$$

$$\begin{aligned}
 \frac{\partial U}{\partial q_{i+n}} &= \sum_{j=1}^{2n} K_{i+n,j} q_j \\
 &= \text{Sting elastic restoring moment at point } x_i
 \end{aligned}
 \tag{21b}$$

2.5.4 The Non-Conservative Generalized Forces

Equation (12) provides for the arbitrary representation of time varying generalized forces (Q_k) that may drive and/or damp the system motion. Q_k is a non-conservative force or moment which essentially means that it is not derived from a potential function such as potential energy (Section 2.5.3). For example, dissipative effects such as sting-model aerodynamic damping and sting structural damping are clearly in this category.

2.5.4.1 Unsteady Aerodynamics

In the present application, the primary driving force (Q_k) is created by unsteady aerodynamic phenomena. The resulting aerodynamic loads may be obtained by

1. Theoretical analysis - Refs. 10 and 11 discuss and critique the available theoretical efforts. Basic trends are reasonably well defined for ideal configurations.

2. Experimental measurements - Good experimental data are highly desirable and should be utilized when available (see Section 3.2).
3. Approximate analysis utilizing both theoretical and experimental information - Practical requirements for unsteady aerodynamic simulation of realistic configurations may dictate such an analysis.

The following quasi-steady approximations are used in the present formulation. For $k = i$, the aerodynamic normal force is

$$Q_i = N_{T_i} = q_\infty S_i C_{N_{T_i}} \tag{22}$$

where q_∞ may vary with time and $C_{N_{T_i}}$ is composed of both a "static" and "dynamic" contribution as follows:

$$C_{N_{T_i}} = \underbrace{[C_{N_i}(\alpha_{T_i})]}_{\text{Static Force Coefficient}} + \underbrace{C_{N_{\dot{\alpha}_i}} \left(\frac{\dot{\alpha}_{T_i}^d}{2V_\infty} \right) + C_{N_{q_i}} \left(\frac{q_{r_i}^d}{2V_\infty} \right)}_{\text{Dynamic Force Coefficient}} \tag{23}$$

If $C_{N_i}(\alpha_{T_i})$ is linear, then

$$C_{N_i}(\alpha_{T_i}) = C_{N_{\alpha_i}} \alpha_{T_i} \tag{24}$$

If nonlinear, then C_{N_i} is curve fitted to a suitable function of α_{T_i} . In a similar manner for $k = i + n$, the aerodynamic moments are

$$Q_{i+n} = M_{T_i} - AF_i [x_i \theta_i - (z_1 - z_i)] \tag{25}$$

where

$$M_{T_i} = q_\infty S_i d_i C_{m_{T_i}} \tag{26}$$

= aerodynamic pitching moment of mass
(m_i) at point (x_i)

then,

$$C_{m_{T_i}} = \underbrace{[C_{m_i}(\alpha_{T_i})]}_{\text{Static Moment}} + \underbrace{C_{m_{\dot{\alpha}_i}} \left(\frac{\dot{\alpha}_{T_i}^d}{2V_\infty} \right) + C_{m_{q_i}} \left(\frac{q_{r_i}^d}{2V_\infty} \right)}_{\text{Dynamic Damping Moment}} \tag{27}$$

Also, if $C_{m_i}(\alpha_{T_i})$ is linear, then

$$C_{m_i}(\alpha_{T_i}) = C_{m_{a_i}} \alpha_{T_i} \quad (28)$$

Otherwise, it is curve fitted as a function of α_{T_i} . Now α_{T_i} , the instantaneous angle of attack at station x_i along the sting, is:

$$\alpha_{T_i} = \underbrace{a_p + q_{i+n}}_{\substack{\text{Angular} \\ \text{Rotation}}} + \underbrace{\frac{x_i \dot{a}_p - \dot{q}_i}{V_\infty \cos a_p} - \frac{\dot{z}_o}{V_\infty}}_{\text{Plunging Translation}} \quad (29)$$

Also:

$$\begin{aligned} \dot{\alpha}_{T_i} = \dot{a}_p + \dot{q}_{i+n} + \frac{x_i \ddot{a}_p - \ddot{q}_i}{V_\infty \cos a_p} - \frac{(x_i \dot{a}_p - \dot{q}_i) V_\infty}{V_\infty^2 \cos a_p} \\ + \frac{(x_i \dot{a}_p - \dot{q}_i) \dot{a}_p \sin a_p}{V_\infty \cos^2 a_p} - \frac{V_\infty \ddot{z}_o - \dot{V}_\infty \dot{z}_o}{V_\infty^2} \end{aligned} \quad (30)$$

The rotational part of $\dot{\alpha}_{T_i}$ is \dot{q}_{r_i} which is

$$\dot{q}_{r_i} = \dot{a}_p + \dot{q}_{i+n} = \dot{a}_p + \dot{\theta}_i \quad (31)$$

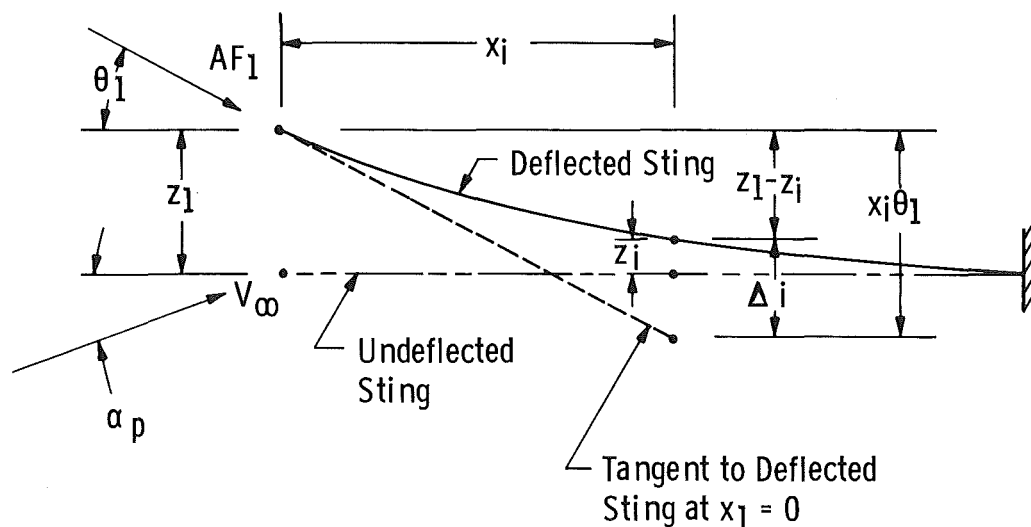
AF_1 is the instantaneous axial force on the model (m_1), which is

$$AF_1 = q_\infty S_1 C_{A_1} \quad (32)$$

The axial force contribution is a stabilizing influence (see Fig. 7) with respect to the beam since its moment apparently acts to reduce deflection, at least for the first mode shape. In most cases, the axial-force moment is largest along the aft and stiffer portion of the sting so that the stabilizing influence is minimized.

The above formulation for C_{N_T} (Eq. (23)) and C_{m_T} (Eq. (27)) is called "quasi-steady" because it implies instantaneous response to α_T . This representation has been used in aircraft-missile trajectory computer programs (Refs. 16 and 17, for instance) with reasonably satisfactory results. It has also been used in Ref. 2 for sting-model motion simulation. Consequently, its use is recommended in the present application unless more precise theoretical and/or experimental information is available. Certain configurations and test conditions may require a more sophisticated aerodynamic force and moment representation.

Inclusion of the angular rate ($\dot{\alpha}_{T_i}$ and q_{r_i}) dependent aerodynamic forces and moments has a negligible effect on motion amplitude and decay for the relatively stiff stings commonly employed in standard static stability and control testing. However, attention must be focused on their influence in dynamic stability testing when a highly sensitive dynamic balance is utilized.



$$\text{Axial Force Moment} = AF_1 [x_i \theta_1 - (z_1 - z_i)]$$

Figure 7. Axial force bending moment schematic.

2.5.4.2 Structural Damping

Observation of experimental sting motion data obtained from the VKF Tunnel F (Section 3.2) revealed that the motion was highly damped. This timewise decrease in amplitude was much more than could be accounted for by aerodynamic damping alone. An investigation revealed that the decrease in amplitude was essentially linear with increasing time. This manner of amplitude decay is normally associated with Coulomb or friction damping (Ref. 9) and the single degree of freedom differential equation is of the form:

$$m\ddot{x} + Kx = -F \frac{\dot{x}}{|\dot{x}|} \quad (33)$$

F is a constant friction force and always acts to oppose the motion. Consequently, it was suspected that some form of structural damping capable of dissipating a large amount of energy was prevalent in the VKF Tunnel F sting.

A brief literature survey revealed that there are basically two types of structural damping:

1. Internal damping of a solid homogeneous structural member caused by internal grain structural, plastic strain, magnetic-electrical, or thermal effects (see Ref. 18 for a comprehensive survey), and
2. Damping of joints, connections, or interfaces of the members of a total structure caused by interfacial Coulomb friction and slip (see Refs. 19 and 20).

Reference 20 reports that under optimum circumstances, the energy dissipated in joint slip damping may be large, not only compared with internal damping, but also compared with the total strain energy of the structure. Since the VKF tunnel-sting contained several prominent joints and its motion was highly damped with essentially a linear decay, it is concluded that damping is primarily caused by interfacial Coulomb friction.

Consequently, it is postulated that the sting damping could be modeled in a rather gross manner by the following relations which are somewhat analogous to the Coulomb friction force in Eq. (33). The damping force at x_i is

$$QDF_i = -FCOF_i \left| \sum_{j=1}^{2n} K_{ij} \dot{q}_j \right| \frac{\dot{q}_i}{|\dot{q}_i|} \quad (34a)$$

The damping moment at x_i is:

$$QDM_i = -FCOM_i \left| \sum_{j=1}^{2n} K_{i+n,j} \dot{q}_j \right| \frac{\dot{q}_{i+n}}{|\dot{q}_{i+n}|} \quad (34b)$$

where

$$\sum_{j=1}^{2n} K_{ij} \dot{q}_j$$

and

$$\sum_{j=1}^{2n} K_{i+n,j} \dot{q}_j$$

are the sting elastic restoring force and moment, respectively, at x_i (Section 2.5.3). $FCOF_i$ and $FCOM_i$ are arbitrary constants which are utilized to adjust the fractional magnitudes of the sting elastic restoring forces and moments, respectively, which are resisting the sting motion. They are determined by numerical experimentation and comparison with experimental sting motion damping data (see Section 3.2).

Formulation of a more elaborate mathematical model of sting structural damping than Eq. (34) will require both analytical and experimental results for typical wind tunnel sting joints.

2.5.5 Specific Motion Equations

The specific motion equations of each individual concentrated mass (m_i) of the sting-model system for each of its two degrees of freedom corresponding to the general formulation (Eq. (12)) can now be written by combining appropriate results from Sections 2.5.2, 2.5.3, and 2.5.4.

For $k = i$, Eqs. (18a), (21a), (22), and (34a) are substituted in Eq. (12) to yield the force relation (in the translational z_i direction) for mass (m_i). It is convenient for future purposes to write this equation as follows:

$$m_{11_i} \ddot{q}_i + m_{12_i} (\ddot{q}_{i+n} + \ddot{a}_p) = (\text{RHSF})_i \quad (35a)$$

where:

$$m_{11_i} = m_i \quad (36a)$$

$$m_{12_i} = -[\cos(q_{i+n})(\bar{x}_i m_i) + \sin(q_{i+n})(\bar{z}_i m_i)] \quad (36b)$$

$$\begin{aligned} (\text{RHSF})_i = & (x_i \ddot{a}_p + q_i \dot{a}_p^2 - \ddot{z}_o \cos \alpha_p - \ddot{x}_o \sin \alpha_p) m_i \\ & + [\cos(q_{i+n})(\bar{z}_i m_i) - \sin(q_{i+n})(\bar{x}_i m_i)] (\dot{q}_{i+n} + \dot{a}_p)^2 \\ & - \sum_{j=1}^{2n} K_{ij} q_j + N_{T_i} + QDF_i \end{aligned} \quad (36c)$$

For $k = i + n$, proper combination of Eqs. (18b), (21b), (25) and (34b) yields the moment equation (in the rotational θ_i direction) for mass (m_i). This is:

$$m_{21_i} \ddot{q}_i + m_{22_i} (\ddot{q}_{i+n} + \ddot{a}_p) = (\text{RHSM})_i \quad (35b)$$

where

$$m_{21_i} = m_{12_i} \quad (36d)$$

$$m_{22_i} = I_{y_i} \quad (36e)$$

$$\begin{aligned} (\text{RHSM})_i = & [(\ddot{z}_o - x_i \ddot{a}_p - q_i \dot{a}_p^2) \cos(q_{i+n}) + (\ddot{x}_o + 2\dot{q}_i \dot{a}_p \\ & + q_i \ddot{a}_p - x_i \dot{a}_p^2) \sin(q_{i+n})](\bar{x}_i m_i) + [(\ddot{z}_o - x_i \ddot{a}_p - q_i \dot{a}_p^2) \sin(q_{i+n})] \\ & - (\ddot{x}_o + 2\dot{q}_i \dot{a}_p + q_i \ddot{a}_p - x_i \dot{a}_p^2) \cos(q_{i+n})](\bar{z}_i m_i) - \sum_{j=1}^{2n} K_{i+n,j} q_j \\ & - AF_I[x_i(q_{i+n}) - (q_1 + q_i)] + M_{T_i} + QDM_i \end{aligned} \quad (36f)$$

Equation (35) is comprised of the basic equations which are both statically and dynamically coupled together in the general case. N_{T_i} and M_{T_i} are still in arbitrary form. If N_{T_i} and M_{T_i} , as represented by Eqs. (22), (23), (26), (27), (29), (30), and (31), are substituted appropriately, then:

$$m_{11_i} = m_i + \frac{N_{\dot{a}_i}}{V_\infty \cos \alpha_p} \quad (37a)$$

$$m_{12_i} = -[\cos(q_{i+n})(\bar{x}_i m_i) + \sin(q_{i+n})(\bar{z}_i m_i)] \quad (37b)$$

$$\begin{aligned} (\text{RHSE})_i = & (x_i \ddot{a}_p + q_i \dot{a}_p^2 - \ddot{z}_o \cos \alpha_p - \ddot{x}_o \sin \alpha_p) m_i \\ & + [\cos(q_{i+n})(\bar{z}_i m_i) - \sin(q_{i+n})(\bar{x}_i m_i)] (\dot{q}_{i+n} + \dot{a}_p)^2 - \sum_{j=1}^{2n} K_{ij} q_j \\ & + N_{\dot{a}_i} \left[\frac{x_i \ddot{a}_p}{V_\infty \cos \alpha_p} - \frac{(x_i \dot{a}_p - \dot{q}_i) \dot{V}_\infty}{V_\infty^2 \cos \alpha_p} + \frac{(x_i \dot{a}_p - \dot{q}_i) (\dot{a}_p \sin \alpha_p)}{V_\infty \cos^2 \alpha_p} \right. \\ & \left. - \frac{\ddot{z}_o}{V_\infty} + \frac{\dot{z}_o \dot{V}_\infty}{V_\infty^2} \right] + (N_{\dot{a}_i} + N_{q_i}) (\dot{q}_{i+n} + \dot{a}_p) + FN_i(\alpha_T) + QDF_i \end{aligned} \quad (37c)$$

$$m_{21_i} = \frac{M_{\dot{\alpha}_i}}{V_\infty \cos \alpha_p} - \cos(q_{i+n})(\bar{x}_i m_i) - \sin(q_{i+n})(\bar{z}_i m_i) \quad (37d)$$

$$m_{22_i} = I_{y_i} \quad (37e)$$

$$\begin{aligned} (\text{RHSM})_i &= [(\ddot{z}_o - x_i \ddot{\alpha}_p - q_i \dot{\alpha}_p^2) \cos(q_{i+n}) + (\ddot{x}_o + 2\dot{q}_i \dot{\alpha}_p + q_i \ddot{\alpha}_p \\ &\quad - x_i \dot{\alpha}_p^2) \sin(q_{i+n})](\bar{x}_i m_i) + [(\ddot{z}_o - x_i \ddot{\alpha}_p - q_i \dot{\alpha}_p^2) \sin(q_{i+n}) \\ &\quad - (\ddot{x}_o + 2\dot{q}_i \dot{\alpha}_p + q_i \ddot{\alpha}_p - x_i \dot{\alpha}_p^2) \cos(q_{i+n})](\bar{z}_i m_i) - \sum_{j=1}^{2n} K_{i+n,j} q_j \\ &\quad - AF_1[x_i(q_{i+n}) - (q_1 - q_i)] + M_{\dot{\alpha}_i} \left[\frac{x_i \ddot{\alpha}_p}{V_\infty \cos \alpha_p} - \frac{(x_i \dot{\alpha}_p - \dot{q}_i) \dot{V}_\infty}{V_\infty^2 \cos \alpha_p} \right. \\ &\quad \left. + \frac{(x_i \dot{\alpha}_p - \dot{q}_i)(\dot{\alpha}_p \sin \alpha_p)}{V_\infty \cos^2 \alpha_p} - \frac{\ddot{z}_o}{V_\infty} + \frac{\dot{z}_o \dot{V}_\infty}{V_\infty^2} \right] + (M_{\dot{\alpha}_i} + M_{q_i}) \\ &\quad \times (\dot{q}_{i+n} + \dot{\alpha}_p) + PM_i(\alpha_T) + QDM_i \end{aligned} \quad (37f)$$

Note that $FN_i(\alpha_T)$ and $PM_i(\alpha_T)$ are the "static" aerodynamic force and moments, respectively, which may be nonlinear functions of α_T and other variables as well. In general, curve fitting or table look-up interpolation of these quantities will be required.

2.5.6 Numerical Solution

Equation (35) is a system of $2n$ second-order differential equations which must be solved simultaneously. The general complexity is such that a numerical solution is required. To accomplish this, a computer program (RKAM) documented in Ref. 21 was employed. In order to apply this computer program written for simultaneous first-order differential equations, it is first necessary to solve Eq. (35) for \ddot{q}_i and \ddot{q}_{i+n} explicitly. This yields

$$\begin{aligned} \ddot{q}_i &= \frac{m_{22_i}(\text{RHSF})_i - m_{12_i}(\text{RHSM})_i}{m_{11_i} m_{22_i} - m_{12_i} m_{21_i}} \\ &= \ddot{z}_i \end{aligned} \quad (38a)$$

$$\ddot{q}_{i+n} = \frac{m_{11_i}(\text{RHSM})_i - m_{21_i}(\text{RHSM})_i}{m_{11_i} m_{22_i} - m_{12_i} m_{21_i}} - \ddot{a}_p \quad (38b)$$

$$= \ddot{\theta}_i$$

These are 2n second-order equations of the general form:

$$\ddot{q}_k = f_k(q_i, \dot{q}_j, t) \quad \left\{ \begin{array}{l} j = 1 \dots 2n \\ k = 1 \dots 2n \end{array} \right\} \quad (39a)$$

where the initial conditions are:

$$\begin{aligned} q_k(t_0) &= a_k & \left\{ \begin{array}{l} k = 1 \dots 2n \\ k = 1 \dots 2n \end{array} \right\} \\ \dot{q}_k(t_0) &= b_k \end{aligned} \quad (39b)$$

Equation (39) can be reduced to a system of 4n first-order equations by the following substitution:

$$\dot{q}_k = s_k \quad k = 1 \dots 2n \quad (40a)$$

Then

$$\dot{s}_k = f_k \quad k = 1 \dots 2n \quad (40b)$$

Equation (40) is a set of 4n first-order equations to be solved simultaneously subject to the following initial conditions from Eq. (37b):

$$\begin{aligned} q_k(t_0) &= a_k & k = 1 \dots 2n \\ \dot{q}_k(t_0) &= b_k & k = 1 \dots 2n \end{aligned} \quad (40c)$$

Equations (40a), (40b), and (40c) are in the form required for solution by the RKAM program (Ref. 21). The resulting computer program is hereafter referred to as SMD2NDOF.

The sting rigid body motion variables ($\alpha_p, \dot{\alpha}_p, \ddot{\alpha}_p, \dot{x}_O, \ddot{x}_O, \dot{z}_O,$ and \ddot{z}_O) must be known as a function of time. These variables are required if the sting system moves as a rigid body (for example, during model to tunnel injection or sector rotation). V_∞ and, occasionally, \dot{V}_∞ and q_∞ must be known as a function of time. These transient variables are currently curve fitted by a Fourier Series or a least-squares polynomial and can thus be computed in SMD2NDOF when needed as a function of time. A table look-up interpolation representation may also be employed.

3.0 APPLICATIONS

3.1 HIRT STING DESIGN AND TRANSIENT RESPONSE

References 22 and 23 provide information concerning the Advanced Transonic Transport or the Advanced Technology Transport (ATT) model which is a representative candidate for analysis. Figure 8 illustrates the predicted history of the dynamic pressure in a pilot, high Reynolds number, Ludwig-type wind tunnel. This information is based primarily on experience with such a VKF pilot facility (Ref. 1). Maximum steady-state dynamic pressures ($q_{\infty_{\max}}$) were selected from conditions reported in Ref. 22.

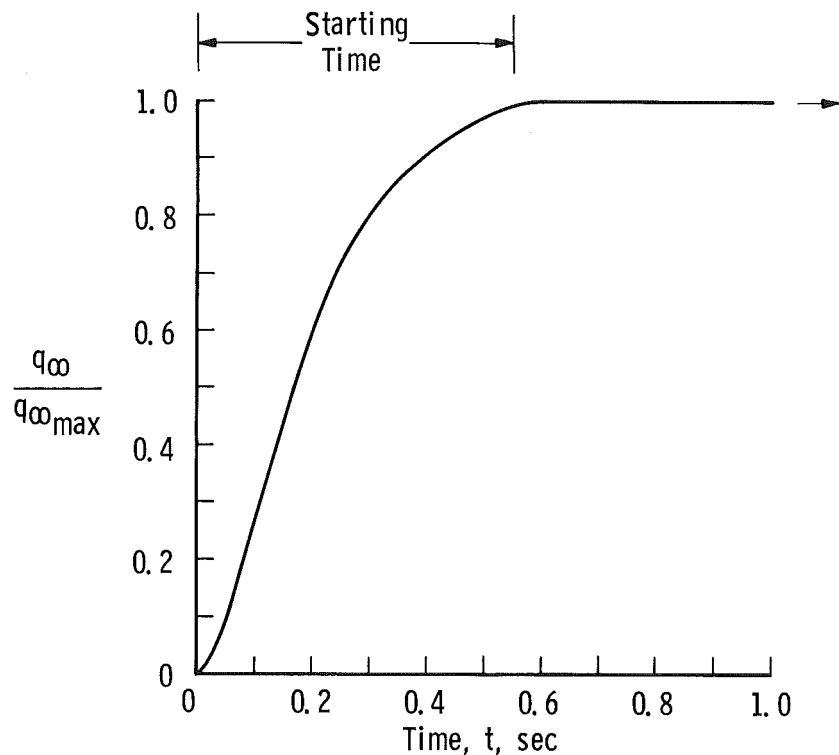
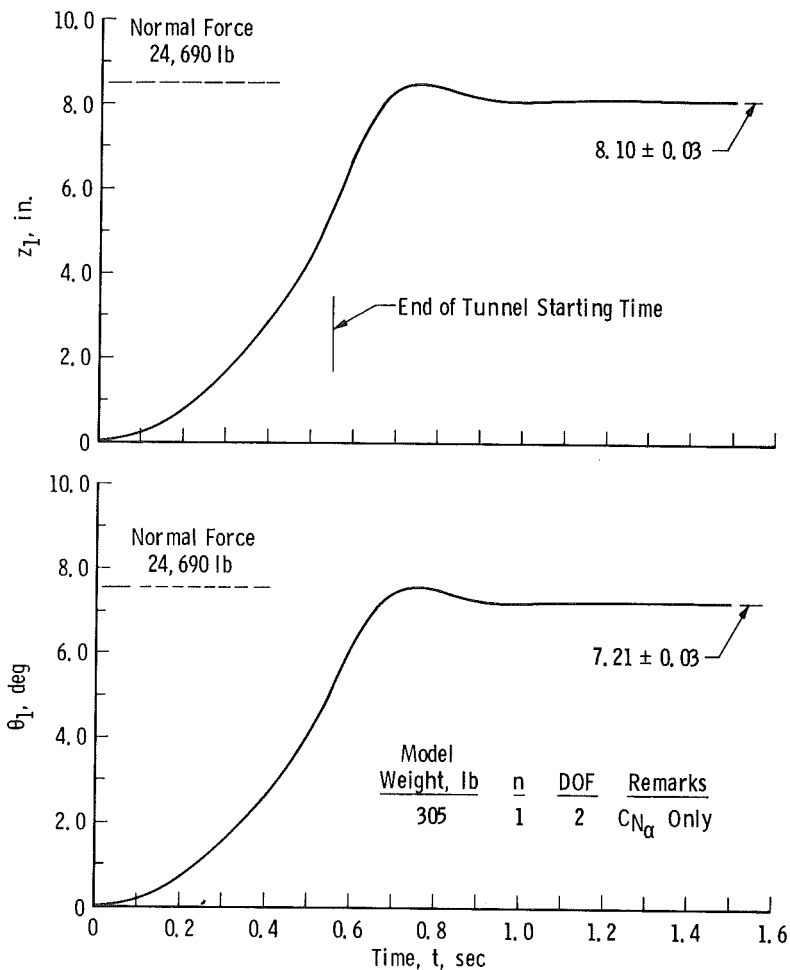


Figure 8. Predicted variation of dynamic pressure ratio in a Pilot Ludweig-Tube Wind Tunnel.

Both the steel sting and the C-S sting were investigated at critical sting design load conditions. One critical point was test condition No. 7 of Ref. 22, Table 2. For this condition, the ATT model at α_T of 8.0 deg generates an aerodynamic normal force of 24,000 lb (see Fig. 3). This

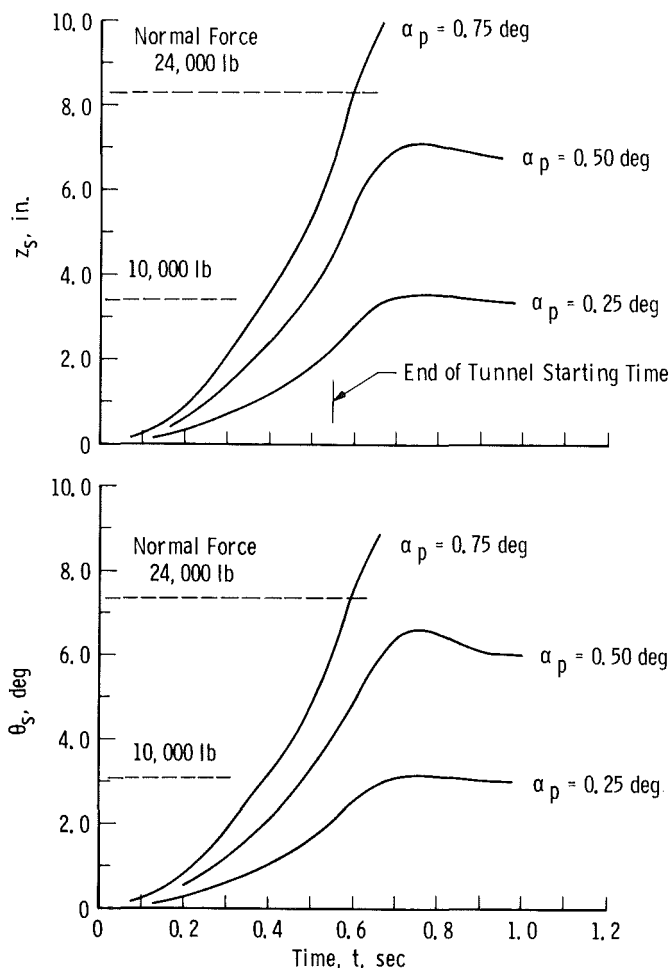
means that α_p (the initial fixed preset angle of the sting, Fig. 6a) plus θ_1 (the angular deflection at the model location) must essentially equal 8 deg. Thus, in order to initially set α_p before the run, $\theta_1(t)$ must be computed.

The steel sting exhibited highly unsatisfactory deflection divergence characteristics under dynamic load conditions. Just a small initial preset angle of attack (α_p) was enough to cause very large sting deflections before the sting strain energy restoring force became sufficient to prevent further deflection (see Fig. 9). The situation is analogous to the torsional divergence of a wing (Ref. 11, Chapter 3). A small increase in α_p from 0.60 to about 0.85 would surely result in catastrophic sting failure. The situation is so unstable that this ATT model could not be tested at this condition with a steel sting.



a. $\alpha_p = 0.60$ deg

Figure 9. Motion history for ATT model and steel sting, condition No. 7, basic q_∞ variation.



b. $\alpha_p = 0.25, 0.50, \text{ and } 0.75$ deg
 Figure 9. Concluded.

Figure 10 illustrates the motion history (θ_1 and z_1 versus time) for the ATT model and the composite C-S sting. Here, α_p is 5.0 deg, and the ATT test condition No. 7 is being simulated. Deflection is less than half of that observed for the steel sting (Fig. 9a); however, this is a critical condition for the carbide portion of the sting ($x \leq 48.5$ in.) because of bending stresses at these loads. Results for two model weights and two different lumped-mass representations ($n = 1$ and $n = 15$) are shown in Fig. 10. For $n = 1$, note that essentially the same results are obtained for both model weights (except for the frequency). The frequencies agree very well with predictions for the C-S sting in Fig. 4, particularly the MATVEC results. For $n = 15$, the sting is represented by 14 lumped masses so that sting inertia is taken into account. This

more complex simulation of the sting makes about 15-percent difference in the results which may be enough to warrant inclusion in some detailed analysis. However, the $n = 15$ results shown required about 7 hr of computation time on the IBM 370/165, whereas the $n = 1$ results required only a few minutes.

Figure 11 illustrates what would happen if the dynamic pressure were a step input for ATT test condition No. 7. Results for two model weights are shown (I_y was held constant). Considerable oscillation is present with the heavier model exhibiting the larger magnitude. It is speculated that the C-S sting would fail catastrophically for this particular step load input condition.

Several computer runs (not illustrated herein) were made with the basic wind tunnel q_∞ variation (Fig. 8) perturbed so as to yield slightly faster initial rise times. The resulting sting oscillation amplitudes were then somewhat more than for the basic q_∞ variation (Fig. 10) but considerably less than for the step q_∞ input (Fig. 11). Both the heavy and light models exhibited practically identical oscillation amplitudes (very low) for the basic q_∞ variation (Fig. 10, $n = 1$). The basic q_∞ (Fig. 8) aerodynamic loading is then essentially like a "static" loading since inertial loads were almost nil. For the step q_∞ input (Fig. 11), the loading was indeed "dynamic" and the heavy and light models did not oscillate at the same magnitudes because of the strong inertial effects. It is worth noting that, if the tunnel dynamic pressure rise time is slower than the basic variation of Fig. 8, then the steady-state run time is decreased accordingly, and very little decrease in sting oscillation amplitude is gained. Consequently, it is concluded that the example wind tunnel's basic q_∞ transient variation was essentially optimum from the viewpoint of both sting oscillation and steady-state run time for model-sting systems of this size.

In lieu of actual experimental transient data, the aerodynamic loads for the ATT were generated from Eqs. (22) and (26) where $q_\infty = q_\infty(t)$. Computer runs were made with reasonable estimates of C_{N_α} , $C_{N_{\dot{\alpha}}}$, C_{N_q} , C_{m_α} , $C_{m_{\dot{\alpha}}}$, and C_{m_q} . It was found, for this particular model and sting attachment point, that only the normal force (C_{N_α}) influenced the sting deflection to any practical extent. This behavior was also noted in a sting-model motion simulation reported in Ref. 2. These stings are so stiff that aerodynamic damping exerts practically no influence. Grossly exaggerated static moment inputs (both stable and unstable via Eq. (28)) did produce noticeable changes in deflection (approximately ∓ 15 percent, respectively).

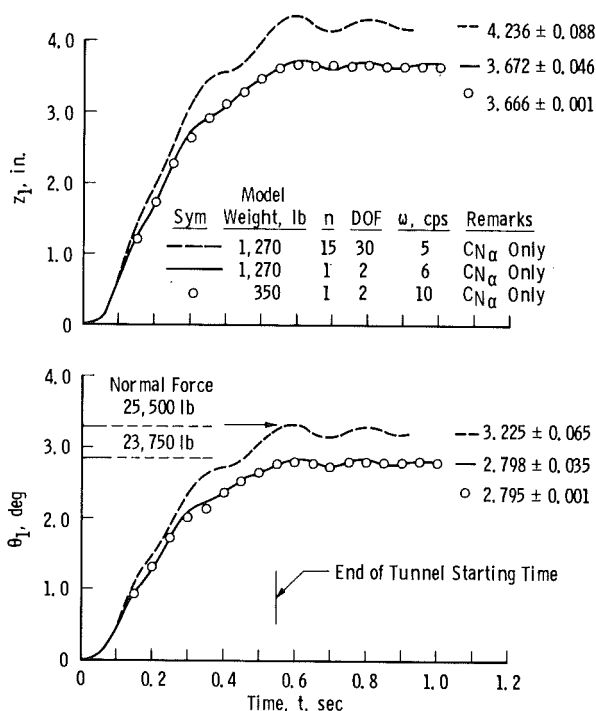


Figure 10. Motion history for ATT model and carbide-steel sting, condition No. 7, basic q_∞ variation, $\alpha_p = 5.0$ deg.

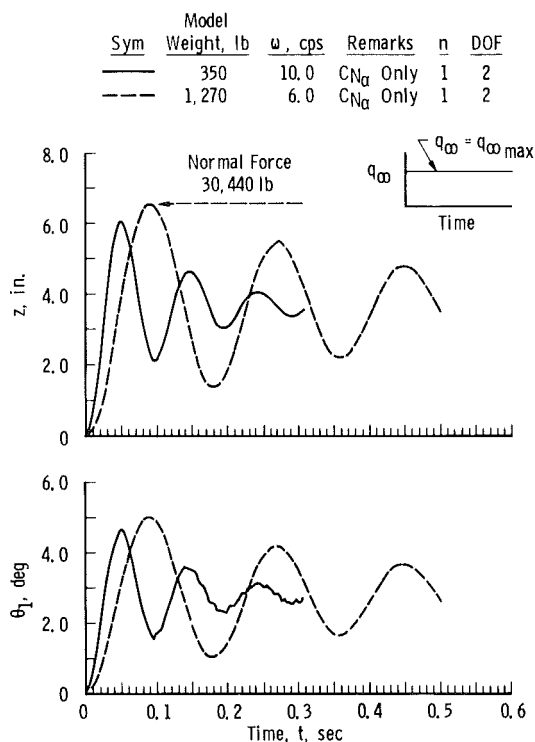


Figure 11. Motion history for ATT model and carbide-steel sting, condition No. 7, $q_\infty = q_{\infty \max}$, $\alpha_p = 5.0$ deg.

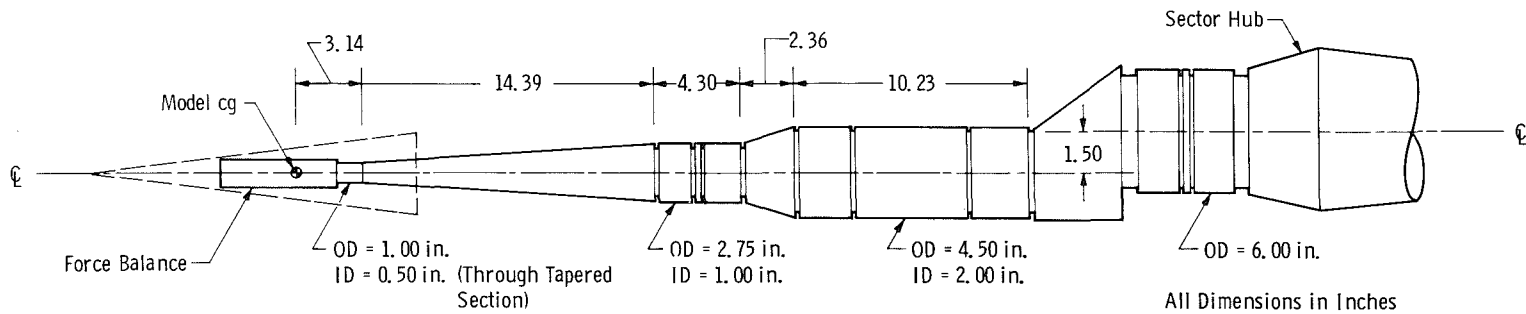
3.2 VKF TUNNEL F STING DYNAMICS

Recent results obtained in VKF Tunnel F have provided an opportunity for comparison with experimental motion data. During this test program, the sting angular deflection was found to be greater than could be accounted for by model aerodynamic loads alone. High-speed motion pictures (framing rate ≈ 4000 frames/sec) were taken during several shots to provide a record of the sting-model deflection. It was speculated that there were significant aerodynamic and inertial loads on the sting itself which contributed to the observed deflection. Consequently, the SMD2NDOF computer program was applied to simulate the sting motion, both with and without sting aerodynamic loads. A general description of the VKF Hypervelocity Tunnel F is contained in Ref. 24.

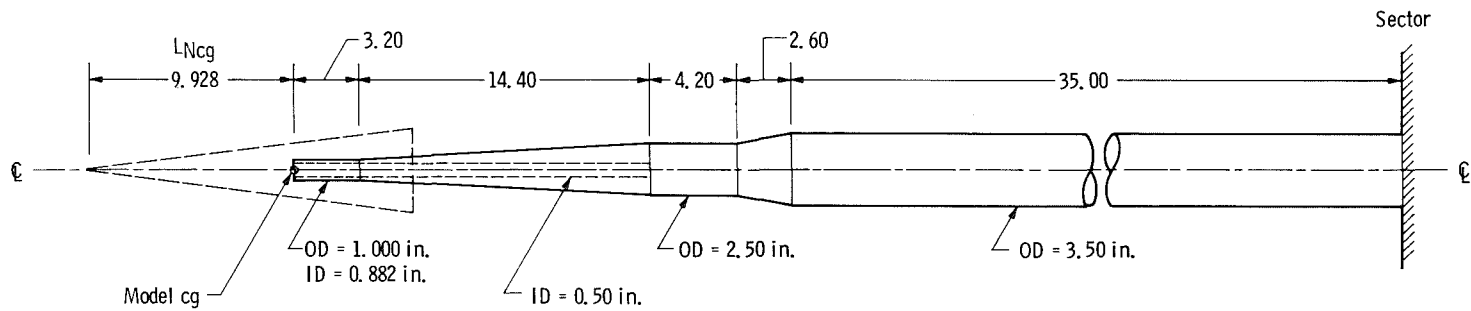
The Tunnel F sting-balance was modeled structurally via the STING-1 program. Some experimental calibration rotational deflection data for the balance alone and the balance plus sting were required to obtain a reasonable stiffness representation of this model support system. The basic sting utilized for this particular test is not as stiff as its exterior dimensions would suggest because of numerous joints and cross-sectional area discontinuities. Figure 12a illustrates the actual sting used during the tests, including the force balance. The general complexity of this actual sting force balance system is such that a number of dimensional iterations were necessary via the STING-1 program to obtain the structural stiffness synthesis illustrated in Fig. 12b. A somewhat more complete synthesis of the sting-force balance system is feasible and should be incorporated in future analyses.

Transient model loads (corrected for inertia effects) were measured during the test. These were curve fitted with a Fourier series and input as forcing functions ($N_{T_1}(t)$ and $M_{T_1}(t)$) to the SMD2NDOF program (Fig. 13). Strictly speaking, the forward and aft normal loads measured by the force transducers in the balance were converted into a normal force and pitching moment which were assumed to act at a single model-balance attachment point (the physical cg location of the model, Fig. 12b). This pitching moment makes a sizable contribution to the sting deflection and cannot be neglected.

Figure 14 illustrates the Tunnel F transient flow velocity history for this particular test.



a. Actual sting configuration



b. Structural stiffness synthesis

Figure 12. VKF Hypervelocity Tunnel F stings.

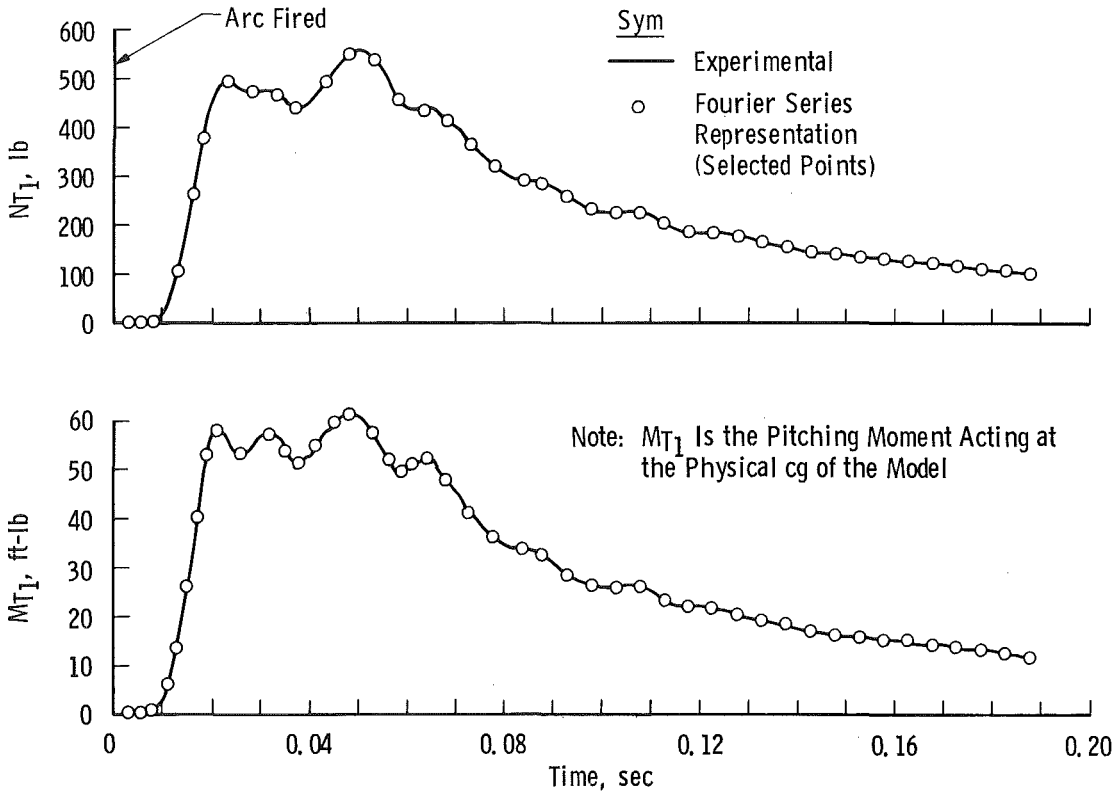


Figure 13. Transient aerodynamic loads on the Tunnel F model.

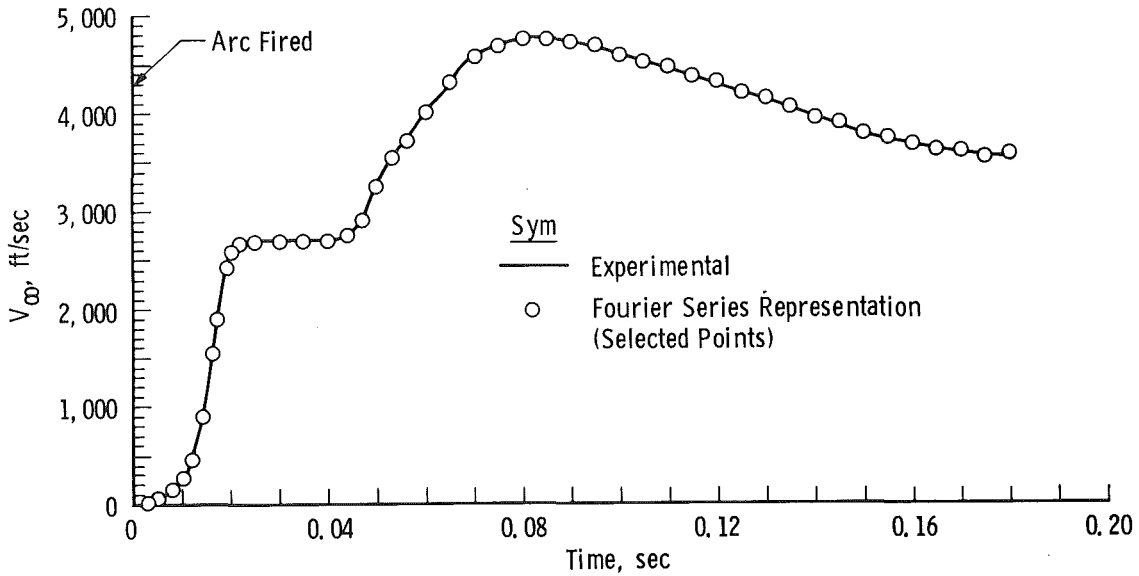


Figure 14. Transient flow velocity history for VKF Tunnel F.

Since airloads on the sting were to be included, the sting was subdivided into 14 sections (concentrated masses, $n = 15$, including the model). No experimental data were available for the aerodynamic loads acting directly on the sting itself. Consequently, these airloads were estimated in the following manner. It was assumed that the airloads (N_{T_i}) on the individual sting masses (m_i) had the same timewise variation as the airload (N_{T_1}) on the model. However, the magnitude of the sting airloads is not equal to model airloads because of different planform areas and different shape effects. The sting is composed of a series of circular cylinders and cone-frustums, while the model is essentially conical. The airload normal force on a cylindrical concentrated mass is then

$$N_{T_i}(t) = \left(\frac{A_{P_i}}{A_{P_1}} \right) \left(\frac{C_{N_i}}{C_{N_1}} \right)_{\alpha \approx 16^\circ} N_{T_1}(t) \quad (41a)$$

where C_{N_1} (model) and C_{N_i} (sting m_i) are based on planform area. C_{N_i} for the sting was estimated from the Newtonian normal force coefficient for circular cylinders (Ref. 25, Chapter 17). The ratio (C_{N_i}/C_{N_1}) remains practically constant from 15 to 17 deg which essentially brackets the observed angles of attack. A_{P_1} and A_{P_i} are the planform areas of the model and m_i , respectively. Planform areas (A_{P_i}) corresponding to the actual sting (Fig. 12a) were employed. For cone-frustum sections of the sting, shape effects were assumed to be similar to those of the model so that

$$N_{T_i}(t) = \left(\frac{A_{P_i}}{A_{P_1}} \right) N_{T_1}(t) \quad (41b)$$

Equations (41a) and (41b) have the general form:

$$N_{T_i}(t) = C_i N_{T_1}(t) \quad (41c)$$

The loads on the sting section were assumed to act at the lumped mass cg and produce no pitching moment ($M_{T_i}(t)$).

Only the last 12 sting masses were considered to be aerodynamically loaded since the two forward portions of the sting are inside the model. The summation of C_i ($i = 4$ to 15) yields the ratio of the sting total normal airload to the model normal airload. In this particular case,

$$\sum_{i=4}^{15} C_i = 3.31 \quad (42)$$

This indicates that the sting airloads are about three times the model airloads. Fortunately, the sting loads are distributed primarily along the stiffer aft sections which alleviates their deflection contribution considerably. The theoretical magnitude of the sting airload contribution to the static deflection can be computed via the deflection influence coefficient approach (Section 2.3). Theoretical results from SMD2NDOF indicate that

$$\frac{\theta_1 \text{ (with sting loads)}}{\theta_1 \text{ (without sting loads)}} \approx 1.12$$

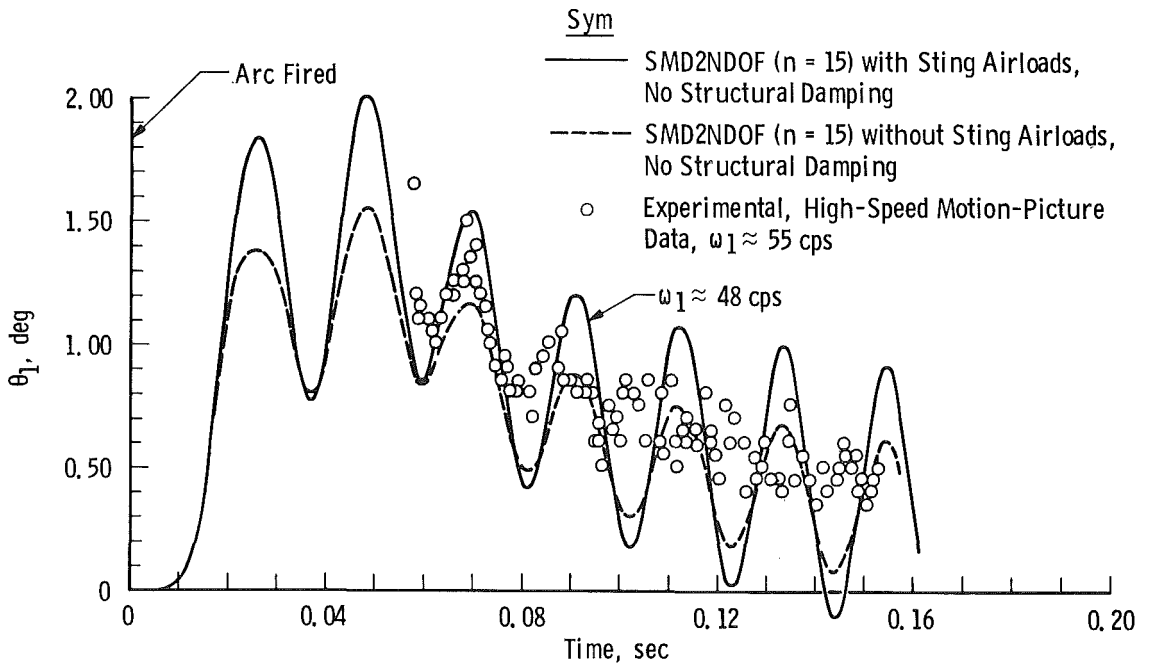
Figures 15 and 16 illustrate both experimental results and SMD2NDOF predictions for this Tunnel F test. Motion predictions were made with and without sting aerodynamic loads. Each prediction requires about 45 min actual computation time on the IBM 370/165. The experimental data (from high-speed motion pictures) are θ_1 (Fig. 15) and z_{nose} (Fig. 16) versus time. z_{nose} was computed by SMD2NDOF as illustrated in Fig. 17.

The predicted dynamic oscillation amplitude (oscillation about the mean or static level, Fig. 15a) is somewhat greater than the experimental magnitude, particularly near the end of the run. It is evident from the experimental data (Figs. 15a and 16a) that considerable damping of the oscillation is occurring. From previous results (Section 3.1), it is known that the damping is structural rather than aerodynamic. Sting structural damping was included in the SMD2NDOF predictions illustrated in Figs. 15b,d and 16b,d. The numerous joints of the actual sting (Fig. 12a) make an important contribution to structural damping (Section 2.5.4.2). This is fortunate from a "static" data accuracy viewpoint and more than compensates for the apparent decrease in stiffness introduced by the joints.

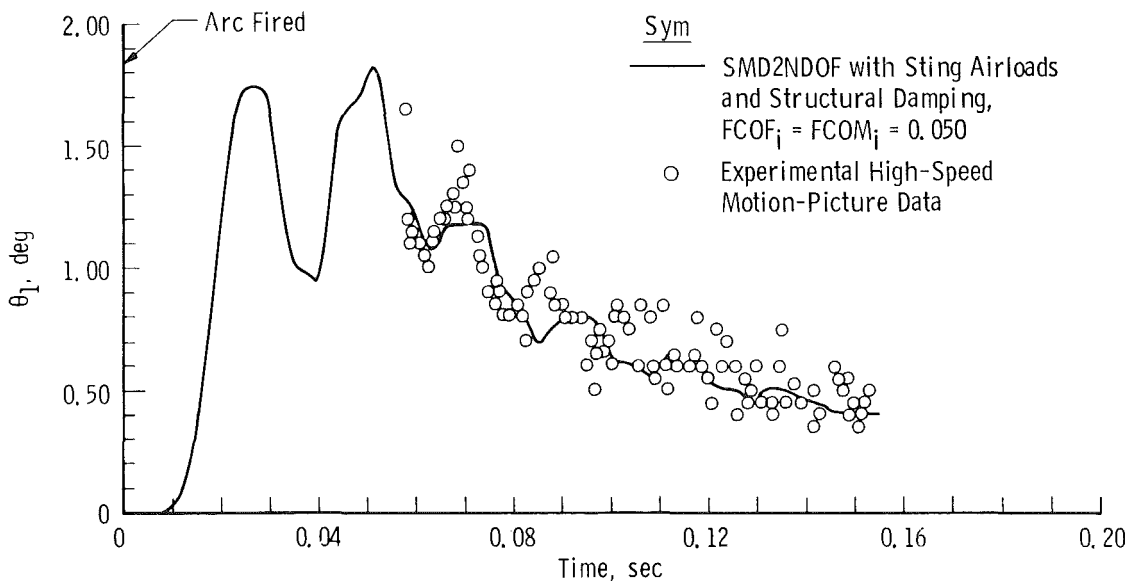
The average magnitude (mean value of the amplitude) of θ_1 versus time is shown in Fig. 15c. Examination of these mean amplitudes reveal a maximum difference of about 0.08 deg between experiment and prediction with sting loads, and about 0.20 deg difference between experiment and prediction without sting loads. The predicted results with sting loads included are in remarkably good agreement with observed magnitudes near the beginning of the run. These results show that it is feasible to account for sting aerodynamic loads on θ_1 (and hence α_{T1}).

There is a slight discrepancy between the predicted (48 cps) and experimental (55 cps) oscillation frequencies. When modeling the sting balance system, the structural stiffness synthesis was of primary

concern, and when those criteria were satisfied, ω_1 was 48 cps for sting-balance plus model (STING-1 program). This was deemed satisfactory since the system frequency was known to be on the order of 50 cps. A large amount of structural damping distorts the sinusoidal amplitude variation considerably (Figs. 15b and 16b) and some discretion is required when computing the frequency from a limited number of cycles of experimental data.

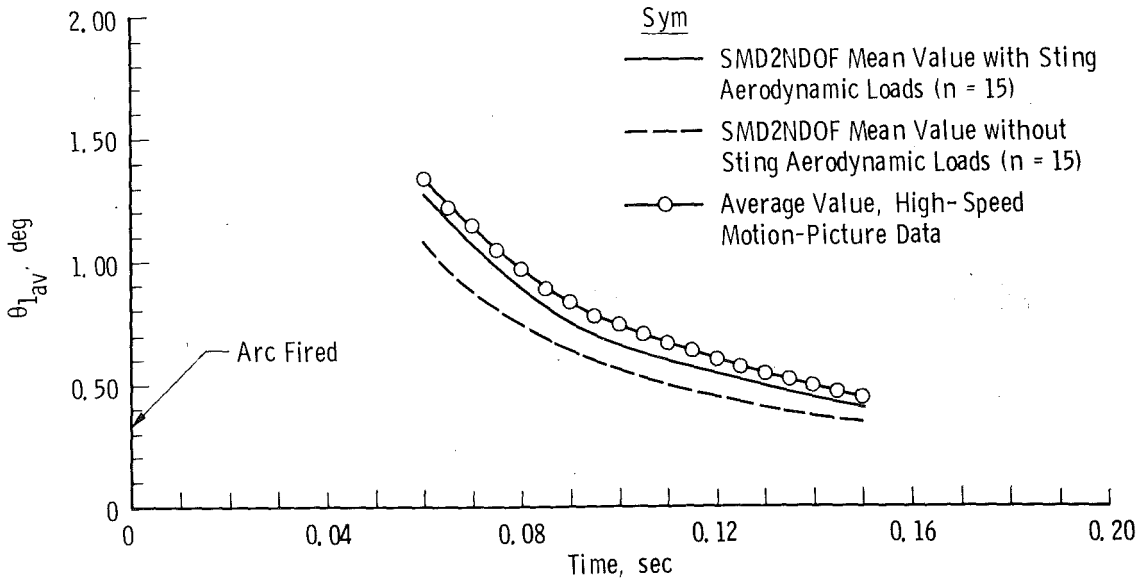


a. Transient amplitude without structural damping

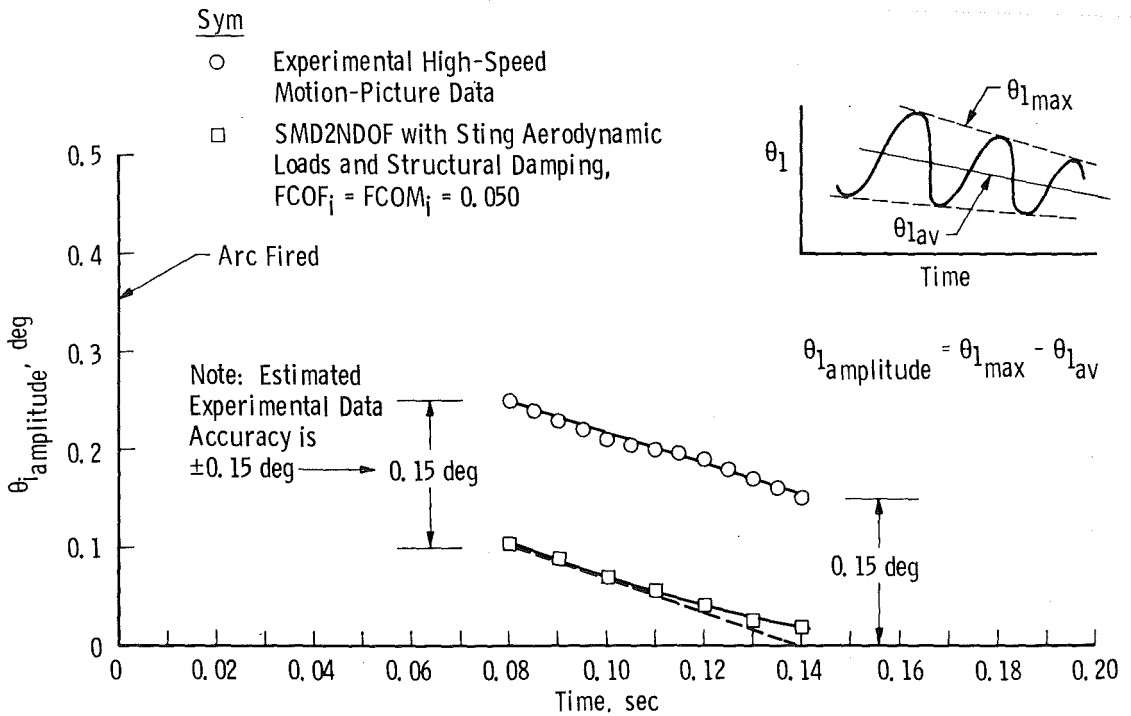


b. Transient amplitude with structural damping

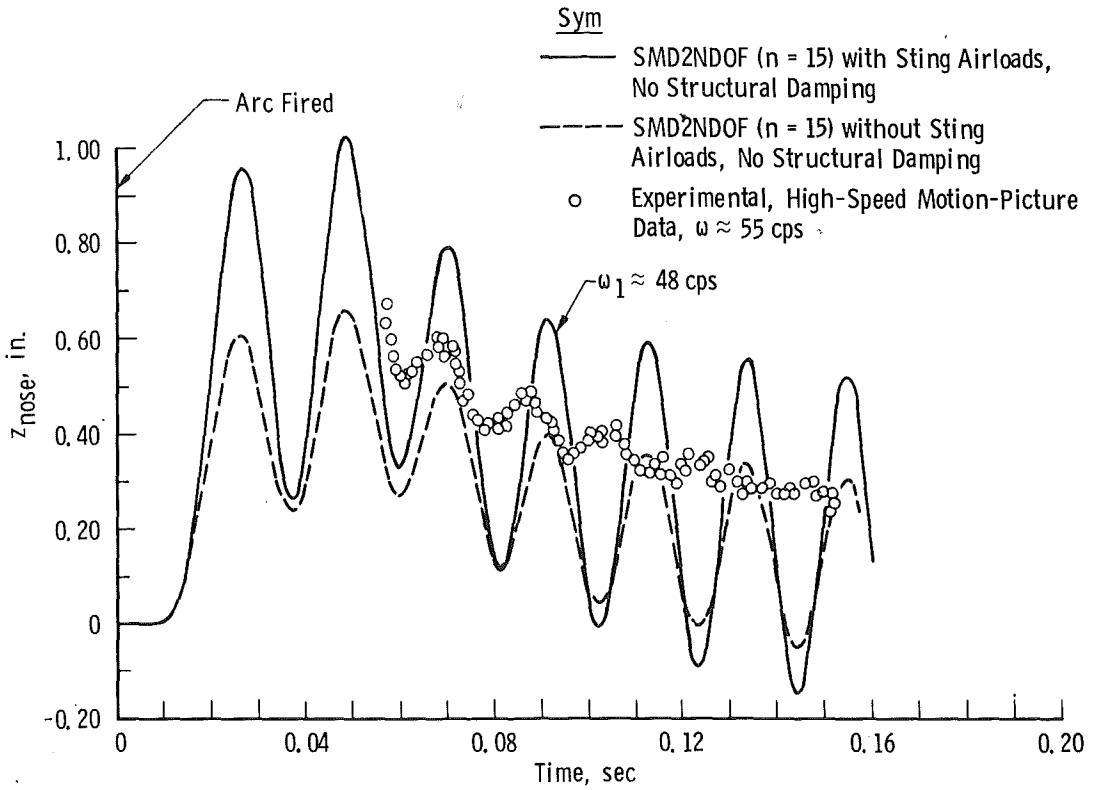
Figure 15. Theoretical and experimental angular deflections of the Tunnel F model.



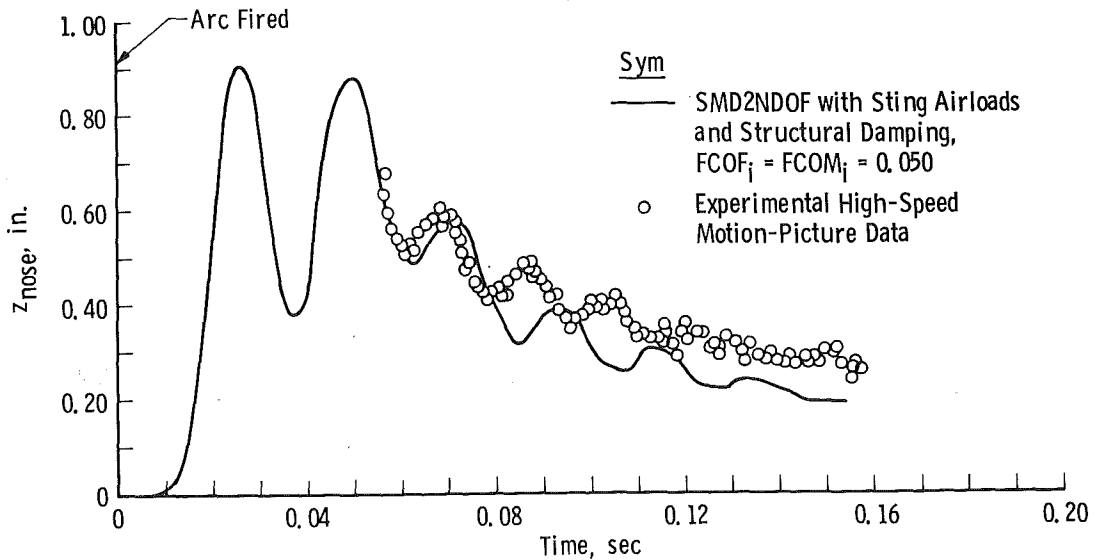
c. Average amplitude



d. Oscillation amplitude
Figure 15. Concluded.

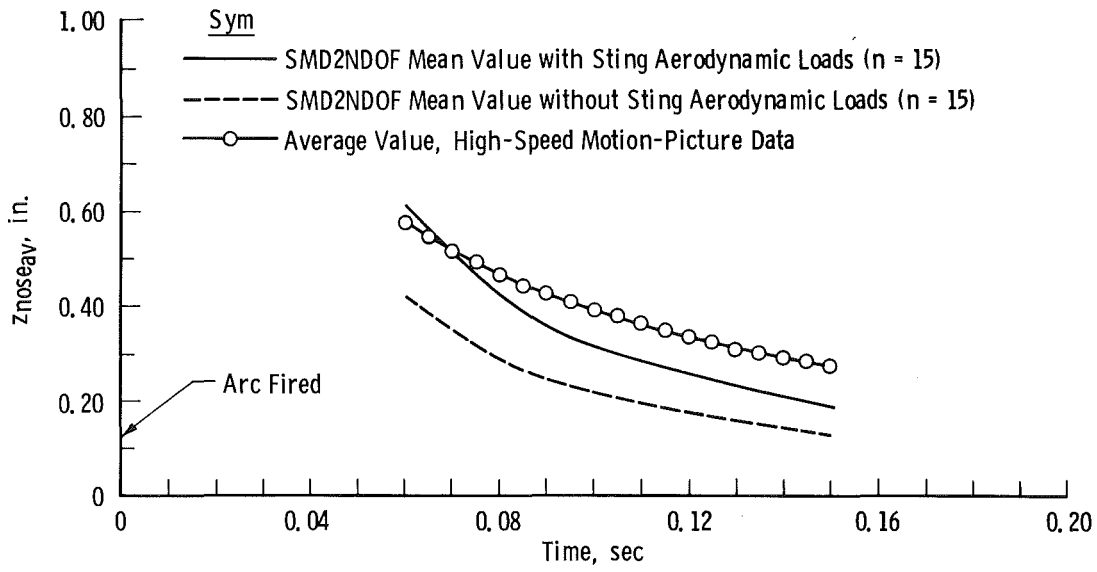


a. Transient amplitude without structural damping

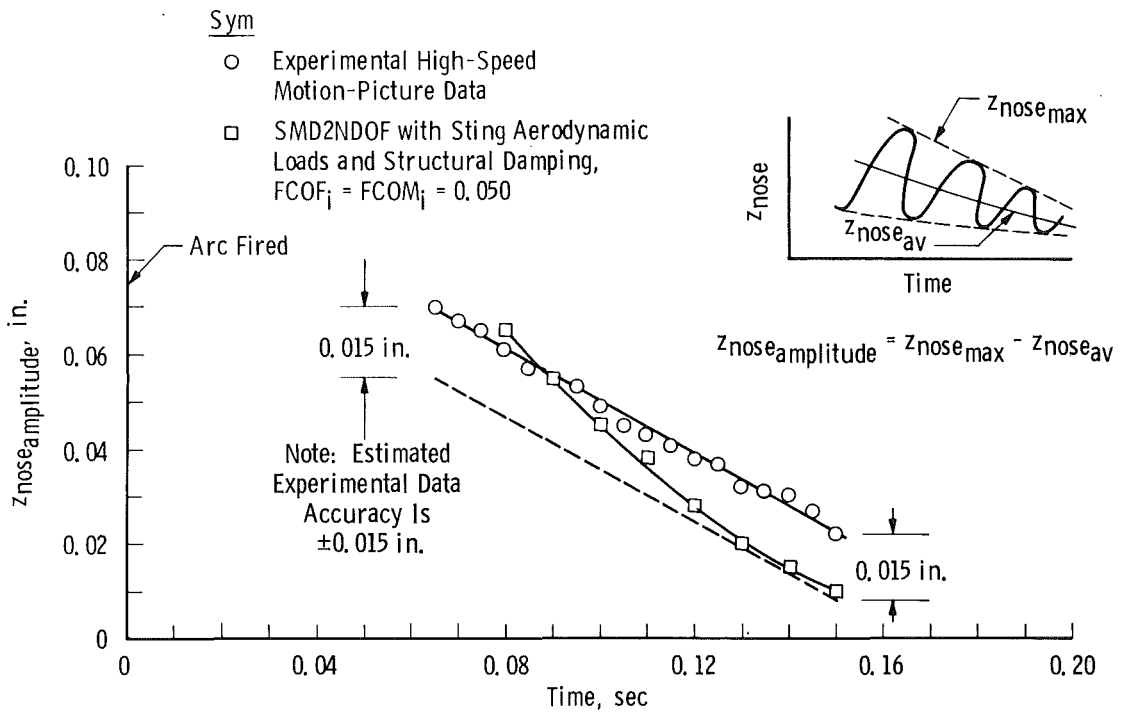


b. Transient amplitude with structural damping

Figure 16. Theoretical and experimental translational model nose tip deflections.



c. Average amplitude



d. Oscillation amplitude
Figure 16. Concluded.

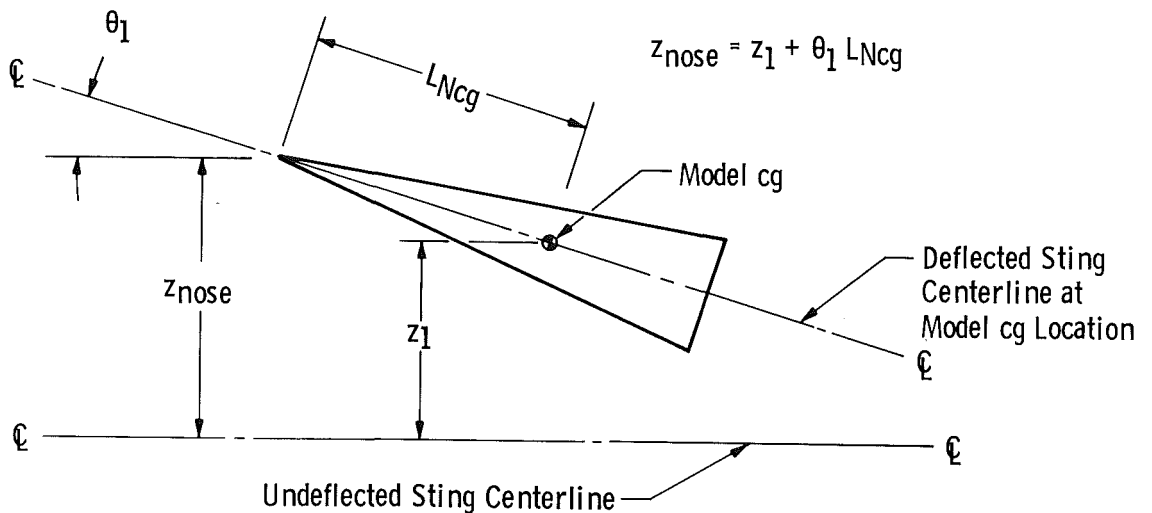


Figure 17. Model nose tip translational deflection geometry.

A realistic assesment of the α_{plunge} magnitude in Tunnel F is of more than academic interest since it is difficult to measure experimentally and it does contribute to the total transient angle of attack of the model (α_{T_1}). From Eq. (29),

$$\alpha_{T_1} = \alpha_p + \theta_1 + \alpha_{\text{plunge}_1} \quad (43)$$

where in the present case,

$$\alpha_{\text{plunge}_1} = - \frac{\dot{z}_1}{V_\infty \cos \alpha_p} \quad (44)$$

Theoretical results (including sting aerodynamic loads and structural damping) for both α_{plunge} and z_1 are illustrated in Fig. 18. The maximum value of the predicted α_{plunge} is approximately one tenth of a degree. Because of the large amount of structural damping present, it is concluded that the maximum α_{plunge} will normally be less than 0.025 deg for force tests in Tunnel F when steady-state data are taken after the initial starting transients.

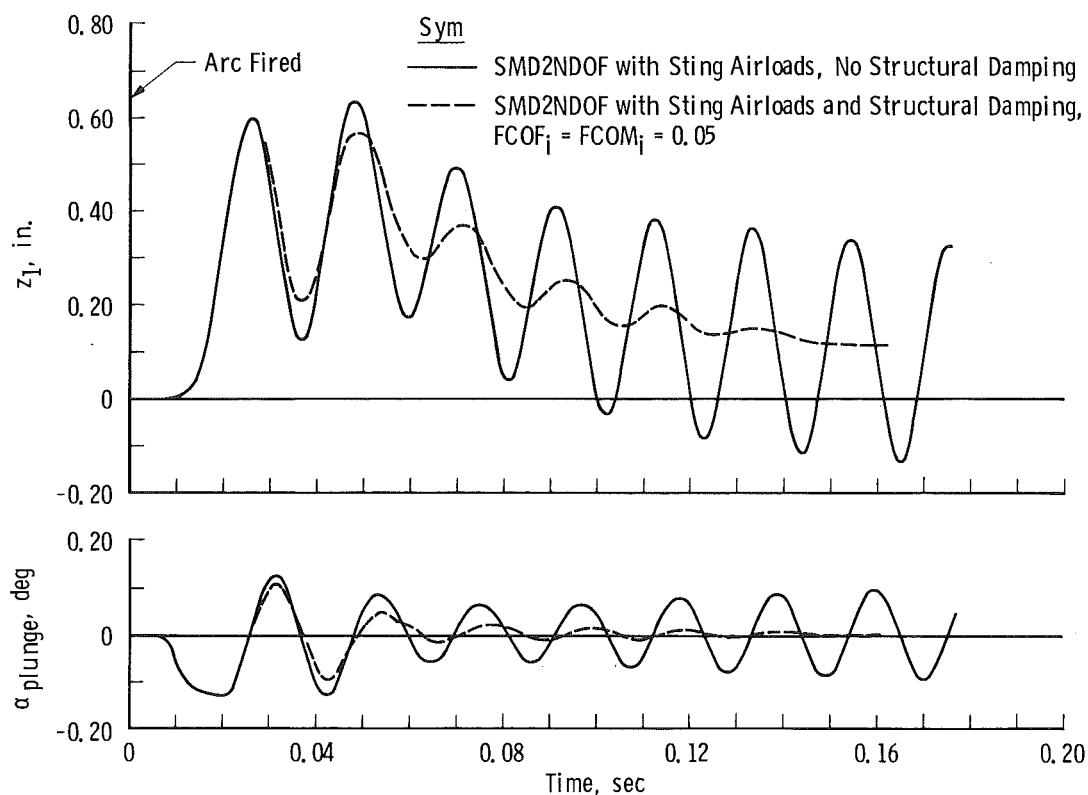


Figure 18. Theoretical results for α_{plunge} and model cg translation (z_1).

4.0 SUMMARY

This investigation of wind tunnel sting structural dynamics has essentially followed two paths. These are:

4.1 STING STRUCTURAL DESIGN

A brief analysis (Section 2.1) has shown that, for a given wind tunnel facility (with fixed dimensions), any real gain in sting stiffness must ultimately come from inherent stiffness properties (E) of the sting material itself. This means that materials stiffer than steel must be considered. Certain carbide alloys (sintered tungsten-titanium carbide) are about three times stiffer than steel and warrant serious attention as a sting construction material. However, any sting material must be able to withstand bending stresses of about $120,000 \text{ lb/in.}^2$. It is not clear that carbide alloys in sting size beams will consistently handle bending stresses of this magnitude. This should be checked by standard experiments.

To assist in structurally analyzing realistic sting configurations, a computer program (STING-1) was written (Section 2.2). With geometrical and material properties as input data, STING-1 computes deflections, first natural frequency, and influence coefficients (spring constants) for cantilever beams with mixed tapered and untapered sections. The material of each section is arbitrary so that a certain type of composite sting may be analyzed. Sting design applications are obvious; however, perhaps the most important application so far has been the computation of structural influence coefficients (Section 2.3) required for certain dynamic analysis procedures (Section 2.4 and 2.5.3). The STING-1 program is based primarily on elementary strength of material concepts but is general and flexible enough to model most of the more common sting-balance configurations.

The MATVEC computer program (Ref. 13) which solves the standard matrix eigenvalue problem is recommended for the computation of sting steady-state vibration natural frequencies and mode shapes. The input required is the $[CTF_{ij} \ m_i]$ matrix (Section 2.4), where both CTF_{ij} and m_i may be computed by the STING-1 program. Prior experience in a structural laboratory with cantilever beams has verified MATVEC predictions.

4.2 STING STRUCTURAL DYNAMICS

Lagrangian mechanics has been employed to derive the coupled differential equations of planar motion for a rather general sting-balance system (Section 2.5). This system is represented by concentrated masses which are tied together by spring constants (influence coefficients) and may be subjected to arbitrary known transient forces and moments. The formulation allows sting loads as well as model loads to be included. Also the system is allowed to move (rotate and translate) as a rigid body. Thus with the proper input, transient conditions occurring during model to tunnel injection and/or sector rotation may be investigated.

The general formulation is such that a numerical solution is required for all but the simplest, almost trivial, cases. Consequently, a standard program (Ref. 21) for solving simultaneous differential equations was employed and modified as required. The resulting program (SMD2NDOF) is versatile enough to simulate a wide variety of sting structural dynamic situations. The sting-model synthesis does not have to be an elaborate multi-mass system to provide useful information. For

example, see Section 3.1 where a single mass representation was employed for the analyzed sting-model. The simulation of the Tunnel F system (Section 3.2) required a more elaborate multi-mass representation since sting aerodynamic loads were to be included.

REFERENCES

1. Starr, R. F. and Schueler, C. J. "Experimental Studies of a Ludweig Tube High Reynolds Number Tunnel." AIAA Paper 73-212, Presented at the AIAA 11th Aerospace Sciences Meeting, Washington, D. C., January 10-12, 1973.
2. Picklesimer, J. R., Lowe, W. H., and Cumming, D. P. "A Study of Expected Data Precision in the Proposed AEDC HIRT Facility." AEDC-TR-75-61 (ADA013814), August 1975.
3. Burt, Glen E. and Uselton, James C. "Effect of Sting Oscillation on the Measurement of Dynamic Stability Derivatives in Pitch and Yaw." AIAA Paper No. 74-612. Presented at the AIAA 8th Aerodynamics Testing Conference, Bethesda, Maryland, July 8-10, 1974.
4. Canu, Michael. "Wind Tunnel Measurement of Aerodynamic Pitch Damping of a Model Oscillating in Two Degrees of Freedom." ERD-TT-72-18 (May). Technical Translation of a report prepared for ONERA, Modane-Avrieux, France.
5. Materials in Design Engineering. Materials Selector Issue. Vol. 64, No. 9, Mid-October 1966, Reinhold Publishing Company, New York.
6. Smithells, C. J. Metals Reference Book. Third Edition, Butterworths, Washington, 1962.
7. Powder Metallurgy. Edited by Werner Leszyneski, Interscience Publishers, New York, 1961.
8. Laurson, P. G. and Cox, W. J. Mechanics of Materials. Third Edition, John Wiley and Sons, Inc., New York, 1954.
9. Thomson, W. T. Mechanical Vibrations. Prentice-Hall, New York, 1954.

10. Bisplinghoff, R. L., Ashley, Holt, and Halfman, R. L. Aeroelasticity. Addison Wesley Publishing Company, Inc., 1957.
11. Fung, Y. C. An Introduction to the Theory of Aeroelasticity. John Wiley and Sons, Inc., New York, 1955.
12. Martin, D. J. and Lauten, T. "Measurement of Structural Influence Coefficients." Chapter 1, Part IV of AGARD Manual on Aeroelasticity. Ed. by R. Mazet, October 1961.
13. Ehrlich, L. "Eigenvalues and Eigenvectors of Complex Non-Hermitian Matrices Using the Direct and Inverse Power Methods and Matrix Deflation." The University of Texas Computation Center, Publication No. UTF4-01-001, August 2, 1961 (Program MATVEC).
14. Wells, Dare E. "Theory and Problems of Lagrangian Dynamics." Schaum's Outline Series, Schaum's Publishing Company, New York, 1967.
15. Goldstein, Herbert. Classical Mechanics. Addison-Wesley Publishing Company, Reading, Massachusetts, 1959.
16. Brown, R. C., Brulle, R. V., Combs, A. E., Vorwald, R. F., and Griffin, G. D. "Six-Degree-of-Freedom Flight Path Study Generalized Computer Program." FDL-TDR-64-1, Part 1, Volume I, and Part 2, Volume I. Prepared by McDonnell Aircraft Corporation for Wright-Patterson AFB, AFFDL, Ohio, October 1964.
17. Brunk, James E. "Users Manual: Extended Capability Magnus Rotor and Ballistic Body 6-DOF Trajectory Program." AFATL-TR-70-40, May 1970, Prepared by Alpha Research, Inc., For AFATL, Eglin, AFB, Florida.
18. Lazan, Benjamin J. Damping of Materials and Members in Structural Mechanics. Pergamon Press, London, 1968.
19. Lazan, B. J. and Goodman, L. E. "Material and Interface Damping (Section on 'Interface Shear Damping')." Shock and Vibration Handbook. Ed. by C. Harris and C. Crede, Vol. II, Chap. 36, McGraw Hill, 1961.

20. Goodman, L. E. and Klumpp, J. H. "Analysis of Slip Damping with Reference to Turbine-Blade Vibration." ASME Journal of Applied Mechanics. Vol. 23, September 1956, pp. 421-429.
21. Lastman, G. J. "Solution of N Simultaneous First Order Differential Equations by Either the Runge-Kutta Method or by the Adams-Moulton Method with a Runge-Kutta Starter, Using Partial Double Precision Arithmetic." UTD2-03-046, January 1964, University of Texas Computation Center (Program RKAM).
22. Alexander, W. K., Griffin, S. A., Holt, R. L., et al. "Wind Tunnel Model Parametric Study for Use in the Proposed 8 ft x 10 ft High Reynolds Number Transonic Tunnel (HIRT) at Arnold Engineering Development Center." AEDC-TR-73-47 (AD763725), March 1973.
23. Holt, R. L., Fatta, G. J., and Tyler, S. P. "Study of Model Aeroelastic Characteristics in the Proposed High Reynolds Number Transonic Wind Tunnel (HIRT) in Reference to the Aeroelastic Nature of the Flight Vehicle." AEDC-TR-75-62 (ADA016797), October 1975.
24. Pate, S. R. and Eaves, R. H., Jr. "Recent Advances in the Performance and Testing Capabilities of the AEDC-VKF Tunnel F (Hotshot) Hypersonic Facility." AIAA Paper No. 74-84, January 30-February 1, 1974.
25. Hoerner, Sighard F. Fluid Dynamic Drag. Busted, New Jersey, 1958.

NOMENCLATURE

Three basic axis systems are used in the sting planar motion analysis of Section 2.5. Figure 6 illustrates these axis systems, and they are further explained as follows:

X_I, Z_I	This is a fixed inertial axis with X_I aligned parallel to V_∞ . The location of the origin is arbitrary.
X_{II}, Z_{II}	This axis is fixed to the undeflected sting and moves (rotates and translates) with the undeflected sting. The origin is at the center of the sector rotation and X_{II} is directed along the undeflected sting centerline. This is the basic axis system from which sting deflections are measured.
X_{III_i}, Z_{III_i}	This axis system is fixed to the i^{th} lumped mass of the system and rotates and translates with this mass. X_{III_i} is tangent to the deflected sting centerline. The origin is arbitrary but if chosen at the mass cg will eliminate terms involving $\bar{x}_i m_i$ and $\bar{z}_i m_i$ in the motion equations.

Additional symbols and nomenclature and abbreviations used herein are defined as follows:

AF_1	Instantaneous axial force on the model, lb, (Eq. (32) and Fig. 8)
A_{p_1}	Planform area of model, ft^2
A_{p_i}	Planform area of the i^{th} mass of the sting, ft^2
ATT	Advanced transonic transport or advanced technology transport.
a_k	Initial value of q_k at $t = t_0$ (Eq. (39b))
b_k	Initial value of \dot{q}_k at $t = t_0$ (Eq. (39b))
C_{A_1}	Instantaneous axial-force coefficient (Eq. (32))
CAF_{ij}	Angular deflection at i caused by unit force at j (Eq. (7))

$C_{AM_{ij}}$	Angular deflection at i caused by unit moment at j (Eq. (7))
C_i	Constant defined by Eq. (41)
C_{ij}	Flexibility influence coefficients (Eq. (6))
C_m	Static aerodynamic pitching-moment coefficient (Eq. (28))
$C_{m\dot{q}_R}$	Aerodynamic pitch damping moment coefficient caused by \dot{q}_R (Eq. (27))
C_{mT}	Total aerodynamic pitching-moment coefficient (Eq. (27))
$C_{m\alpha}$	Slope of static pitching-moment coefficient, $dC_m/d\alpha$ (Eq. (28))
$C_{m\dot{\alpha}}$	Aerodynamic pitch damping moment coefficient caused by $\dot{\alpha}$ (Eq. (27))
C_N	Static aerodynamic normal-force coefficient (Eq. (24))
$C_{N\dot{q}_R}$	Aerodynamic normal-force coefficient caused by \dot{q}_R (Eq. (23))
C_{NT}	Total aerodynamic normal-force coefficient (Eq. (23))
$C_{N\alpha}$	Slope of static normal force coefficient, $dC_N/d\alpha$ (Eq. (24))
$C_{N\dot{\alpha}}$	Aerodynamic normal force coefficient caused by $\dot{\alpha}$ (Eq. (23))
C-S	Carbide-Steel composite sting
CTF_{ij}	Translational deflection at i caused by unit force at j (Eq. (7))
CTM_{ij}	Translational deflection at i caused by unit moment at j (Eq. (7))
c	Distance from beam neutral axis to surface, (Eq. (2)), $c = d/2$ for circular cross-section stings
cg	Center of gravity or, more correctly, center of mass location
DOF	Degrees of freedom (number of independent coordinates necessary to describe motion)

d	Aerodynamic reference length, ft or sting diameter, in.
E	Modulus of elasticity or Young's Modulus, lb/in. ²
E1 to E5	E for beam sections in STING-1 computer program (Fig. 2)
F	Friction force (Eq. (33))
FN	Static aerodynamic normal force, lb ($FN = q_{\infty} S C_N$)
FCOF _i , FCOM _i	Structural damping constants (Eq. (34))
f _k	General functional form of \ddot{q}_k (Eq. (39a))
g	Gravitational constant, lbm/lbf/ft/sec ²
I	Area moment of inertia of beam cross section, in. ⁴ or ft ⁴
ID	Internal diameter of a hole through a sting section, in. (Fig. 12)
I _y	Mass moment of inertia of the model or a discrete lumped mass of the system representation, ft-lb-sec ² (Eq. (17d))
i, j, k	General indices
K	Linear spring constant, force/deflection
K _{ij}	Stiffness influence coefficients (Eq. (8a))
L	Length of sting, in. or ft
L1 to L5	Length of individual sting sections (Fig. 2)
L _{Ncg}	Length from model nose tip to cg position, in. (Figs. 12 and 17)
M	Total bending moment acting on sting at station x, in. -lb, or ft-lb
M _T	Total aerodynamic pitching moment, ft-lb (Eq. (26))
M _q	$(q_{\infty} S d^2 / 2 V_{\infty}) C_{m_q}$
M _α	$(q_{\infty} S d^2 / 2 V_{\infty}) C_{m_{\alpha}}$

m	Mass, lb-sec ² /ft
m_i	Mass of i^{th} system component, lb-sec ² /ft
m_{11i}	Quantity defined by Eqs. (36a) or (37a)
m_{12i}	Quantity defined by Eqs. (36b) or (37b)
m_{21i}	Quantity defined by Eqs. (36d) or (37d)
m_{22i}	Quantity defined by Eqs. (36e) or (37e)
N	Number of DOF, $N = 2n$ in the analysis of Section 2.5
N_T	Total aerodynamic normal force, lb (Eq. (22))
$N1$ to $NEND$	Station numbers in STING-1 program (Fig. 2)
N_q	$(q_\infty S d/2 V_\infty) C_{Nq}$
N_α	$(q_\infty S d/2 V_\infty) C_{N\alpha}$
n	Number of lumped or concentrated masses employed in system representation
OD	Outer diameter of sting, in.
PM	Static aerodynamic pitching moment, in.-lb or ft-lb ($PM = q_\infty S d C_m$)
Q_k	Non-conservative generalized force (or moment) (Section 2.5.4)
QDF_i	General structural damping force, lb (Eq. (34a))
QDM_i	General structural damping moment, ft-lb (Eq. (34b))
q_k	Generalized independent deflection coordinate, used also with various indices such as i , j , or $i + n$
\dot{q}_k	dq_k/dt
\ddot{q}_k	d^2q_k/dt^2
q_r	$\dot{\alpha}_p + \dot{\theta}$, rotational portion of $\dot{\alpha}_T$, radian/sec
q_∞	Free-stream dynamic pressure which may be a transient quantity, lb/ft ²
$q_{\infty \text{max}}$	Maximum value of q_∞ , lb/ft ²
$RH1$ to $RH5$	Hole radius in sting sections, STING-1 Program, in. (Fig. 2)

$(RHSF)_i$	Right-hand side of i^{th} force Eq. (35a) (Eqs. (36c) or (37c))
$(RHSM)_i$	Right-hand side of i^{th} moment Eq. (35b) (Eqs. (36f) or (37f))
$R(N1)-R(NEND)$	Radius at sting section discontinuities in STING-1 Program, in. (Fig. 2)
S	Reference area, ft^2
s_k	\dot{q}_k , (Eq. (40a))
\dot{s}_k	\dot{f}_k , (Eq. (40b))
T	Total kinetic energy of sting-model system, ft-lb (Section 2.5.2)
T_i	Kinetic energy of the i^{th} mass of the system representation, ft-lb (Section 2.5.2)
t	Time, sec
t_0	Initial time, usually taken as zero before transient conditions begin, sec
U	Total potential energy of the sting-balance system, ft-lb (Section 2.5.3)
V_{ABS}	Absolute velocity of a particle of mass (dm), ft/sec (Section 2.5.2)
V_∞	Free-stream tunnel velocity which is allowed to be a transient quantity, ft/sec. V_∞ must be known to compute α_{plunge} .
W_i	Weight of a concentrated mass, lb
W_M	Weight of model, lb
$W1$ to $W5$	Specific weights of sting section material in STING-1 program, $\text{lb}/\text{in.}^3$ (Fig. 2)
w	Specific weight of sting material, $\text{lb}/\text{in.}^3$
x	General coordinate along undeflected sting centerline measured from sector rotation point, in.; also general distance coordinate
x_0	Horizontal location of X_{II} , Z_{II} axis origin with respect to the X_I , Z_I axis origin, ft

\dot{x}_O	Horizontal velocity component of X_{II} , Z_{II} axis (sting-model system moving as a rigid body), ft/sec
\ddot{x}_O	Horizontal acceleration component of X_{II} , Z_{II} axis, ft/sec ²
x_i	x_{II_i} , location of i^{th} mass measured along undeflected sting centerline from model attachment point, in. (Eq. (16c), Fig. 6)
\bar{x}_i	Location of cg of mass (m_i) with respect to X_{III_i} , Z_{III_i} origin, ft (Eq. (17b), Fig. 6c)
x_{Ip}	Horizontal location of particle of mass (dm) with respect to X_I , Z_I axis origin, ft (Eq. (14a), Fig. 6c)
x_{II_i}	x_i , location of i^{th} mass measured along undeflected sting centerline along X_{II} from X_{II} , Z_{II} axis origin, ft (Eq. (16c), Fig. 6)
x_{III_i}	Location of particle of mass (dm) with respect to X_{III_i} , Z_{III_i} origin, ft, (Fig. 6b)
z	General deflection coordinate of sting centerline, measured perpendicular to undeflected sting centerline, in.
z_O	Vertical location of X_{II} , Z_{II} axis origin with respect to the X_I , Z_I axis origin, ft
\dot{z}_O	Vertical velocity X_{II} , Z_{II} axis (sting-model system moving as a rigid body), ft/sec
\ddot{z}_O	Vertical acceleration component of X_{II} , Z_{II} axis, ft/sec ²
z_i	Z_{II} or q_i , deflection of i^{th} mass relative to undeflected sting centerline, in. (Eq. (16a), Fig. 6) also normalized deflections (eigenvectors) in Eq. (11)
\dot{z}_i	$d\dot{z}_i/dt$ or \dot{q}_i , ft/sec
\ddot{z}_i	d^2z_i/dt^2 or \ddot{q}_i , ft/sec
\bar{z}_i	Location of cg of mass (m_i) with respect to X_{III_i} , Z_{III_i} axis origin, ft (Eq. (17c), Fig. 6c)

z_{Ip}	Vertical location of particle of mass (dm) with respect to X_I , Z_I axis origin, ft (Eq. (14b), Fig. 6c)
z_{IIi}	z_i or q_i , deflection of i^{th} mass with respect to X_{II} axis, in. (Eq. (16a), Fig. 6)
z_{IIIi}	Location of particle mass (dm) with respect to X_{IIIi} , Z_{IIIi} axis origin, ft (Fig. 6b)
z_{av}	Average amplitude of z , ft or in.
z_{max}	Maximum amplitude of z_i , ft or in.
z_{nose}	Amplitude of model nose tip translation, in. (Fig. 17)
$z_{amplitude}$	Oscillation amplitude of z , ft or in., ($z_{amplitude} = z_{max} - z_{av}$)
α_p	Pitch angle of sting-model acting as a rigid system (rotation of X_{II} , Z_{II} axis), deg or rad
$\dot{\alpha}_p$	Angular rate of X_{II} , Z_{II} axis rotation, rad/sec
$\ddot{\alpha}_p$	Angular acceleration of X_{II} , Z_{II} axis, rad/sec ²
α_{plunge}	Angle of attack caused by transverse plunging velocity components, deg or rad (Eqs. (29), (43), and (44))
α_T	Total angle of attack, deg or rad (Eq. (29))
$\dot{\alpha}_T$	$d\alpha_T/dt$, rad/sec (Eq. (30))
Δ_i	Moment arm of axial force, ft ($\Delta_i = x_i\theta_i - z_1 + z_i$) (Fig. 7)
ϵ_b	Maximum bending strain at station x , in/in., (Eq. (3))
θ_i	q_{i+n} , rotational deflection of sting at station x_i , deg or rad (Eq. (16b))
$\dot{\theta}_i$	\dot{q}_{i+n} , rad/sec
$\ddot{\theta}_i$	\ddot{q}_{i+n} , rad/sec ²
θ_{iav}	Average amplitude of θ_i , deg
θ_{imax}	Maximum amplitude of θ_i , deg

$\theta_{i\text{amplitude}}$	Oscillation amplitude of θ_i , deg ($\theta_{i\text{amplitude}} = \theta_{i\text{max}} - \theta_{i\text{av}}$)
Λ	$1/\omega^2$, (CTF _{ij} m _i) matrix eigenvalue, (Eq. (11))
σ_b	Maximum bending stress at station x, lb/in. ² (Eq. (2))
σ_y	Material yield stress, lb/in. ² (Table 1)
ω_i	Frequency of vibration of the i th mode, cps (i = 1, 2, 3, etc.)